# “Light takes no shortcuts”

Frequency dependence of the controlled propagation of light in random scattering materials

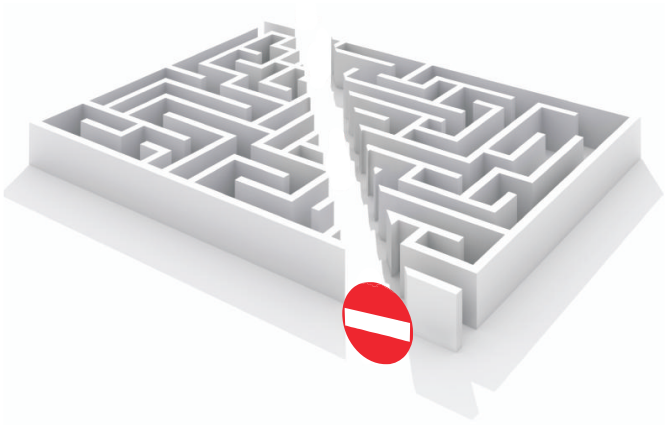

Frerik van Beijnum
Master’s Thesis
Applied Physics, University of Twente
February, 2009

# "Light takes no shortcuts"

Frequency dependence of the controlled propagation of light in random scattering materials

Master's Thesis
Master of Science, Applied Physics
Frerik van Beijnum
February 2009

**Graduation committee:**
E.G. van Putten, M.Sc. (COPS)
Dr. A.P. Mosk (COPS)
Prof. dr. A. Lagendijk (COPS and AMOLF)
Prof. dr. J.L. Herek (Optical Sciences)

**This work was done at COPS:**
Complex Photonic Systems
MESA$^+$ Institute for Nanotechnology
Faculty of Science and Technology
University of Twente
P.O. Box 217
7500 AE Enschede

# FOKKE & SUKKE

WERKEN OP DE NATUURKUNDEFACULTEIT

# Acknowledgements

In April 2008, all I knew about my thesis work were the two main ingredients, so called phase plates and a tuneable laser. This rare combination gave a whole new range of opportunities. Being young, ambitious and naive, I wanted to do it all. Fortunately, many people helped, inspired, and coached me, which has lead to wonderful results.

In the course of the project I enjoyed my cooperation with Elbert, Allard and Ad. Elbert had a strong influence on the thesis, especially his revisions of the theory chapter boosted the quality. To me, his most important contribution was the way he could relate to the issues I had. Allard puts a lot of humor and excitement in our work. The fact that his door is literally always open is something I strongly value. Ad inspired me to think about the actual meaning of our research. Ad also taught me how to present the work and convince others it is relevant. Last, I would like to acknowledge Elbert, Allard and Ad for their quick revisions of my chapters.

The COPS group was very supportive and inspiring throughout the entire project. Chair holder Willem Vos managed to make an important remark on every poster I presented, which is a talent I admire. Moreover he enabled the entire project by making the MBR laser available to me. The COPS members created a pleasant environment, in which many more people will thrive. Danang, Bas, Karen, Niels, Philip, Rajesh, and Willem Tjerkstra, thank you. Cock, thank you for co-designing the impressive sample holder. Hannie, you were of great support in the chemical lab and I think you personally spiced COPS up. Ivo, thank you for all the work you have done and your admirable thesis. Léon, thank you for our valuable discussions on the sample fabrication, and for throwing your T-shirts away. I am also very grateful to Jennifer Herek, chair holder of the Optical Sciences group, for thoroughly reviewing my thesis and being part of the graduation committee.

The monthly East-West meetings were very exciting, seeing other people's work and getting a lot of feedback makes you feel part of a team, I thank you all. I thank Ramy for our discussions on writing a thesis and doing research. Timmo, thank you for your comments on the sample fabrication and the $TiO_2$ you shared. Tom, Sanli, and Elbert, thank you for your work on the Latex template.

Moreover I want to thank my friends at E.S.G. Bogh for distracting me from my work. I thank my family for supporting me to go to Twente, it was a choice I will never regret. Lot, I hope you will always be with me and support me the way you did the past nine months.

Frerik

# Abstract

The average propagation of light in random scattering materials is described by diffusion theory. For a single instance of disorder large intensity fluctuations exist. This random intensity pattern, called speckle, is caused by interference. By shaping the phase and amplitude of the incident light, it is possible to enhance the intensity of a speckle up to a factor of 1000. The goal of our research is to determine what the mechanism is behind this intensity enhancement. The propagation of light inside a random scattering medium is described by infinitely many paths inside the sample. It is possible that wavefront shaping selects short and stable paths inside the material, or all paths contribute and enhanced speckles are then described by transport theory.

We performed experiments in which we measured the intensity decay of an enhanced speckle when the frequency of the incident light is detuned. We compared the result with an experimentally determined $C^1$ correlation function, and we found good agreement, as expected from transport theory. The combination of our experiments with results we derived from transport theory, shows that wavefront shaping is fully described by transport theory.

# Contents

Chapter 1

# Introduction

## 1.1 Diffusion of light

Diffusion is an everyday phenomenon. The smell of a fresh baked bread diffuses through your kitchen. When a tea bag is doped in water, the color of the tea spreads according to diffusion. The red glance seen if your finger is illuminated by a white light source is caused by the diffusion of light.

One can imagine diffusion as a particle bouncing around between other particles, the particle can be an atom, electron, photon or any other particle. The bouncing of particles is called scattering. Scattering of light is caused by a change in the refractive index. If light is scattered multiple times it will lose its direction. The diffusion of light differs from the diffusion of atoms because light is a wave. Light interferes and therefore, when coherent light is used, the scattered light has a random intensity pattern called speckle.

## 1.2 Controlling diffusion

In previous work (see e.g. [1, 2]) it was shown that the wave character of light opens new doors in the diffusive process. Recently it was shown that it is possible to shape the incident wavefront such that one creates an intense focus with the multiple scattered light [3, 4]. This focus is the result of the constructive interference of the waves transmitted through the sample. In analogy with the smell of the fresh baked bread, the focus would be a very strong scent of fresh baked bread, at a specific location in your kitchen, whereas you would hardly smell it elsewhere.

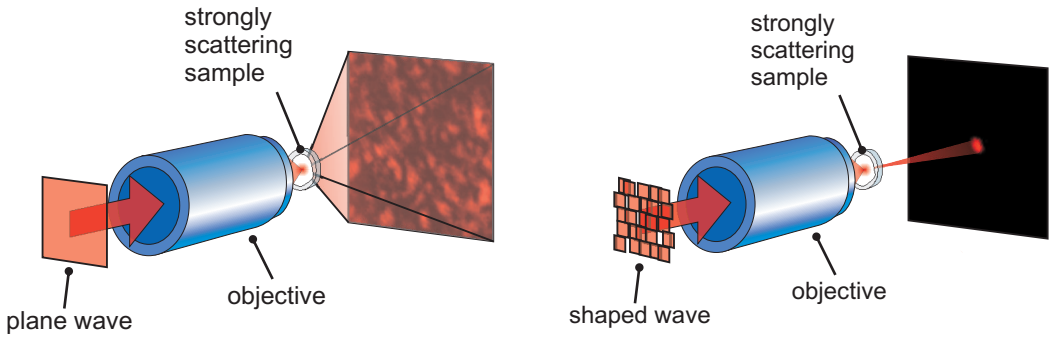


*(a)* *(b)*

*Figure 1.1: An illustration of the principle of wavefront shaping. (a) A plane monochromatic wave is focussed on a random scattering sample. The transmitted light propagates in all directions and random intensity fluctuations are seen. (b) A spatially shaped wavefront is focussed onto the same sample. An intense focus is seen with respect to the background intensity. Illustrations created by dr. I.M. Vellekoop*

The experiments performed are done on many kinds of strongly scattering media. For example in white paint, a human tooth and chicken. Although these samples are opaque, they still transmit a small fraction of the incident light. This small portion of transmitted light is controlled such that an intense focus was made.

We illustrated the technique in Fig. 1.1. In the left illustration we see what happens when a plane monochromatic light wave is focussed on a strongly scattering medium. The transmitted light is spread over a large area, and random intensity fluctuations are seen. In the right illustration we see what happens when a spatially shaped wavefront is focussed on the sample. We now see a focus behind the sample, with an intensity much larger than the background intensity. To find the optimum wavefront a feedback algorithm is used.

There are some interesting questions left concerning this technique. There was no direct evidence that all light waves are controlled inside the sample. One can expect that all paths in the random scattering material contribute as predicted by transport theory. This possibility is illustrated in Fig. 1.2. The left picture shows a variety of paths in the scattering sample of which all paths, independent on the length or field, contribute equally to the focus. On the other hand these paths could be uncontrollable due to their complexity or length and therefore they would not contribute to the focus. This results in the right hand side illustration, which shows only a few paths contributing to the focus. In these short paths the light is mainly scattered in the forward direction.

In this thesis we present measurements which can show whether the width of the distribution of paths remains the same when a focus is created. In this measurement we create a focus behind a strongly scattering medium, and thereafter we detune the frequency of the incident light. If the distribution of paths is very narrow, i.e. all the paths have approximately the same length, the focus will only decay after a very large detuning of the laser frequency. If this is the case, it is very likely that this narrow distribution of

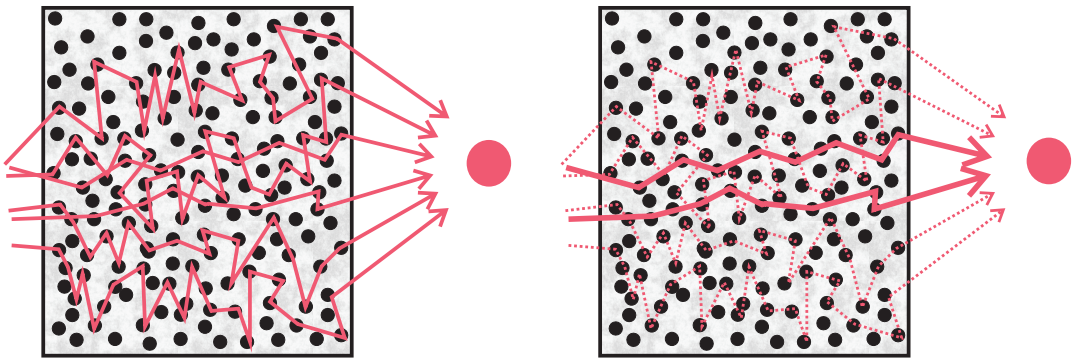

*(a)* *(b)*

*Figure 1.2: An artist impression of the two possible scenario which both lead to an enhanced speckle. (a) All the paths from the source to the target speckle contribute to the enhanced speckle. (b) Only the short paths contribute o the enhanced speckle.*

paths consists mostly of very short paths, since these paths are most stable. If the paths contributing to the focus are not different than those contributing to any other speckle, the intensity will decay similar to average speckles.

## 1.3 Outline of this thesis

In this thesis we first review the relevant theory which is required to understand the experiments performed (Chapter 2). In the theory we also develop a prediction of the decay of the focus. Moreover we will show, in theory, whether it is possible to artificially construct a focus which decays very slowly, or very rapidly. In this thesis the focus is referred to as an enhanced speckle.

In Chapter 3 we present the setup, which is the first setup in which the frequency can be detuned together with the creation of an enhanced speckle. The samples made for our experiments are discussed in Chapter 4. We end this thesis with the results of the experiments in Chapter 5 and the conclusions and discussion in Chapter 6.

# Chapter 2

# Theory

## 2.1 Introduction

In the experiments presented in this thesis, we combine wavefront shaping with a laser which has a tunable frequency. This chapter reviews the required theory to understand wavefront shaping experiments. Since there is no theory available for wavefront shaping in the frequency domain, we extend the existing theory.

We will introduce the fundamental quantities describing the propagation of light in random scattering materials in Section 2.2. Correlation functions [5] will be discussed to describe the frequency dependence of light without wavefront shaping (Section 2.3). The chapter will be concluded with a description of the theory for wavefront shaping experiments in the frequency domain (Section 2.4).

## 2.2 Light transport in random media

In our experiments many general concepts of the propagation of light in random scattering media are used, these concepts will be introduced in this section. We first describe a single scattering event, before we derive the quantities describing multiple scattering. The diffusion constant will be introduced, and the diffusion equation will be solved in a slab geometry. We will introduce the scattering channels, transmission coefficients and phase delay times to gain a qualitative understanding of speckle.

### 2.2.1 Single scattering

To understand multiple scattering, single elastic scattering events will be treated first. Light is scattered when it encounters a change in index of refraction in space. If spatial fluctuations in the index of refraction are much larger than the wavelength, scattering can be described by geometrical optics. A spherical disturbance in the order of a wavelength, for example a small water droplet in the fog, is described by Mie scattering. The interaction of light with spheres and cylinders of arbitrary size can be solved analytically using Maxwell's equations [6].

Scattering by particles much smaller than the wavelength of light, is described by Rayleigh scattering. Fine powder grains and molecules are considered to be Rayleigh scatterers. Rayleigh scattering describes the interaction of light with an electric dipole polarizability, and therefore the interaction between light and a Rayleigh scatterer is polarization dependent. [6]

In this work we consider elastic scattering. In the case of elastic scattering the light and atom are excited into a so-called virtual state. This virtual state has zero probability to be detected, and therefore the photon is emitted immediately. The atom is now back in its ground state. Therefore there is a direct correspondence between the phase of the incident light and the phase of the scattered light.

In the case of inelastic scattering the atom is excited to a real excited state. This means there is a nonzero probability of finding the atom in this state, and there is no direct correspondence between the phase of the incident light and the emitted light. If the light is absorbed and re-emitted, the emitted photon can be of a different frequency than the incident light, this will cause the phase correspondence to be lost.

The probability of scattering light is determined by the scattering cross section $\sigma_s$, which has units of length$^2$. The total power, integrated over all angles, of scattered light is given by the product of the intensity and $\sigma_s$. The scattering cross section depends on the size of the particle with respect to the wavelength and the refractive index contrast of the scatterer with respect to the medium the scatterer is in.

### 2.2.2 Multiple scattering

In the multiple scattering regime there are three important lengths, namely: the scattering mean free path, the transport mean free path and the absorption length. The average distance between two consecutive scattering events is the scattering mean free path $\ell_\mathrm{s}$, which is determined by the number density of scatterers $\rho$ and the scattering cross section $\sigma_s$:

$$\ell_\mathrm{s} = (\rho\sigma_s)^{-1}. \tag{2.1}$$

In the limit where $\ell_\mathrm{s}$ is smaller than the thickness of the scattering medium, multiple scattering occurs.

Some properties of multiple scattering can be derived by using a random walk approximation. To describe the propagation of light as a random walk, two consecutive steps in the random walk have to be independent of each other. The scattered light is independent of the incident light if the average direction after scattering is zero. We will now define

the average distance light has to travel before it has no average direction anymore, the transport mean free path.

The Poynting vector defines the direction of light. A weighted average over the cosine of all scattering angles $\langle\cos\theta\rangle$ defines the magnitude of the average Poynting vector after scattering. After one scattering mean free path a fraction of $(1-\langle\cos\theta\rangle)$ of the incident light has no average direction. The fraction of light which takes two scattering mean free paths before it has no average direction anymore is $\langle\cos\theta\rangle(1-\langle\cos\theta\rangle)$. The average distance after which all the light has lost its direction is thus a weighted average over all path lengths and is defined by:

$$\begin{aligned} \ell_{\mathrm{tr}} &\equiv \ell_{\mathrm{s}}(1-\langle\cos\theta\rangle)\sum_{n=0}^{\infty}(n+1)\langle\cos\theta\rangle^{n} \\ &= \frac{\ell_{\mathrm{s}}}{1-\langle\cos\theta\rangle}. \end{aligned} \tag{2.2}$$

For Rayleigh scatterers $\langle\cos\theta\rangle = 0$, and therefore its transport mean free path will be equal to the scattering mean free path.

To model absorption, we introduce the absorption length $\ell_{\mathrm{a}}$ which is the distance light can travel in a material before it is attenuated to $1/e$ of its original intensity. The amount of steps in a random walk needed to traverse that distance is the fraction of $\ell_{\mathrm{a}}$ and $\ell_{\mathrm{tr}}$. In a random walk, the light is normally distributed after many scattering events. If the light has traveled a distance $\ell_{\mathrm{a}}$, the light is spread with a standard deviation of $L_a$:

$$L_a = \sqrt{\frac{\ell_{\mathrm{a}}\ell_{\mathrm{tr}}}{3}}. \tag{2.3}$$

The length $L_a$, called the diffusive absorption length, is thus the net distance light travels before it is attenuated to $1/e$ of the original intensity [1]. The albedo $a$ is defined as the amount of scattered light divided by the amount light removed due to absorption. This can be written in terms of the absorption length and the transport mean free path [1]:

$$a = 1 - \frac{\ell_{\mathrm{tr}}}{\ell_{\mathrm{a}}} \tag{2.4}$$

In terms of the albedo $L_a$ is [7]:

$$L_a = \frac{\ell_{\mathrm{tr}}}{\sqrt{3(1-a)}}. \tag{2.5}$$

### 2.2.3 The diffusion constant

The diffusion constant is a crucial quantity if one performs dynamic experiments, i.e. experiments where the frequency changes. The purpose of this section is to show how the diffusion constant determines the distribution of light in space and time. Moreover we discuss how the transport mean free path depends on the diffusion constant, and what the relation is between the diffusion constant and the average time light spends in the material.

The propagation of light is determined by the location of the scatterers. Because the exact location of scatterers is unknown, an exact prediction of the light propagation is impossible. By averaging over different sample realizations the average distribution of light inside a random scattering medium can be calculated. The average propagation of a continuous wave inside a scattering medium is described by the stationary diffusion equation (see e.g. [8]):

$$-D\nabla^2 u(\mathbf{r}) = S(\mathbf{r}), \tag{2.6}$$

where the energy density $u(\mathbf{r})$ has units $[\frac{\mathrm{J}}{\mathrm{m}^3}]$ and the source $S(\mathbf{r})$ has units power density $[\frac{\mathrm{W}}{\mathrm{m}^3}]$ [2, 9]. The diffusion constant depends on $\ell_{\mathrm{tr}}$ and the energy velocity $v_{\mathrm{e}}$:

$$D = \frac{v_{\mathrm{e}}\ell_{\mathrm{tr}}}{3}. \tag{2.7}$$

The energy velocity is usually equal to the phase velocity, though it can strongly decrease in the neighborhood of resonances of the scatterers [10, 11].

As discussed before, the position after a random walk of $n$ steps is approximately Poisson distributed. The standard deviation of the distribution will be $\sqrt{n}\ell_{\mathrm{tr}}$. Thus if a distance of $L$ needs to be traversed, a order of $(L\ell_{\mathrm{tr}})^2$ scatter events are required. The average time in between two consecutive steps in the random walk is given by $\ell_{\mathrm{tr}}/v_{\mathrm{e}}$. The average time light spends inside the medium to travel a net distance $L$, is thus in the order of:

$$\tau_{\mathrm{d}} = \frac{L^2}{D}. \tag{2.8}$$

This time scale is known as the Thouless time. The Thouless is sometimes defined with a prefactor, depending on the location of the source inside the medium [12] and the number of dimensions.

### 2.2.4 Diffusion in a slab

Our experiments will be performed on a finite slab of random scattering material. To see how light diffuses through such a slab, we will now solve the diffusion equation in a slab geometry. With this solution we can determine the amount of transmitted light.

The diffusion equation describes an infinite random scattering medium. To solve the diffusion equation for a slab geometry boundary conditions are required and a source needs to be defined. We will now use the boundary condition of energy conservation to describe the behavior at the edge of the random scattering material. If energy is conserved, the energy density current across an infinitely small closed surface has to be equal to the added energy per unit time inside the surface. In differential form this can be written as:

$$-\nabla\mathbf{J}(\mathbf{r}) = S(\mathbf{r}), \tag{2.9}$$

where $\mathbf{J}(\mathbf{r})$ is the energy current. The energy current is also known as the specific intensity [2]. Assuming a stationary situation, this equation can be combined with Eq. 2.6 and we find:

$$\mathbf{J}(\mathbf{r}) = -D\nabla u(\mathbf{r}) \quad \text{for } \mathbf{r} \neq \mathbf{r_s}, \tag{2.10}$$

which is called Fick's law.

The second boundary condition required is the source. We assume an infinitely thin source of diffusive light at a distance $\ell_{\rm tr}$ from the border of the sample. If the source is assumed to be an infinite plane, the problem becomes one dimensional. The expression for the source now reads $S_0\delta(z-\ell_{\rm tr})$ [9].

The current at the sample interfaces can be analyzed. There will be a current $J\mathbf{e_z}$ directed towards the interface, of which $-\bar{R}J\mathbf{e_z}$ is reflected back into the sample. Here $\bar{R}$ is the Fresnel intensity reflection coefficient averaged over all angles [13], and $\mathbf{e_z}$ is the unit vector in $z$-direction. The net current at the sample interface will be:

$$\begin{aligned}\mathbf{J}(\mathbf{r}{=}\mathbf{0}) &= (1-\bar{R})J\mathbf{e_z} = -D\nabla u(\mathbf{r}{=}\mathbf{0}), &(2.11)\\ &= -D\frac{\partial u}{\partial z}|_{\mathbf{r}=\mathbf{0}\mathbf{e_z}}, &(2.12)\end{aligned}$$

where Fick's law was used, along with the fact that we use an infinite plane as a source.

The energy density $u(\mathbf{r})$ is given by the integral:

$$u(z) = \frac{1}{v_{\rm e}}\int_0^{2\pi}\int_0^{\pi} d\theta d\phi \sin(\theta)\mathbf{J}(\mathbf{r})\cdot\mathbf{s}. \tag{2.13}$$

Here the energy current is integrated over all directions $\mathbf{s}$, which is a unit vector. Because the energy current flows at the rate of the energy velocity, the integral has to be divided by this speed. Since we are dealing with a one dimensional problem, the integral reduces to a sum over two directions. For the energy density we find:

$$u(\mathbf{r}) = \frac{1}{v_{\rm e}}(1+\bar{R})\mathbf{J}(\mathbf{r})\cdot\mathbf{s} = \frac{1}{v_{\rm e}}(1+\bar{R})J. \tag{2.14}$$

The $J$ terms can be equated, which leads to the following boundary condition:

$$u(\mathbf{r}) - z_{\rm e1}\frac{\partial u}{\partial z} = 0, \tag{2.15}$$

where $z_{\rm e1} \equiv \ell_{\rm tr}\frac{2}{3}\frac{1+\bar{R}}{1-\bar{R}}$, which is the so called extrapolation length [14, 15]. From this boundary condition one can see that the extrapolation length is the distance at which the intensity can extrapolated to zero outside the sample. For the interface at $z = L$ a similar approach leads to:

$$u(\mathbf{r}) - z_{\rm e2}\frac{\partial u}{\partial z} = 0, \tag{2.16}$$

with $z_{\rm e2} \equiv \ell_{\rm tr}\frac{2}{3}\frac{1+\bar{R}}{1-\bar{R}}$, which is the extrapolation length at the right boundary. The reflection coefficient $\bar{R}$ is not necessarily identical for the left and right boundary.

A incident plane wave can be modeled by a infinitely small source at a distance $\ell_{\rm tr}$ from the boundary. This source is mathematically described by a delta function times a source power density $S_0$. To solve the diffusion equation, the left and right hand side of 2.6 are integrated. Integrating the delta function over $z$ once yields the Heaviside step

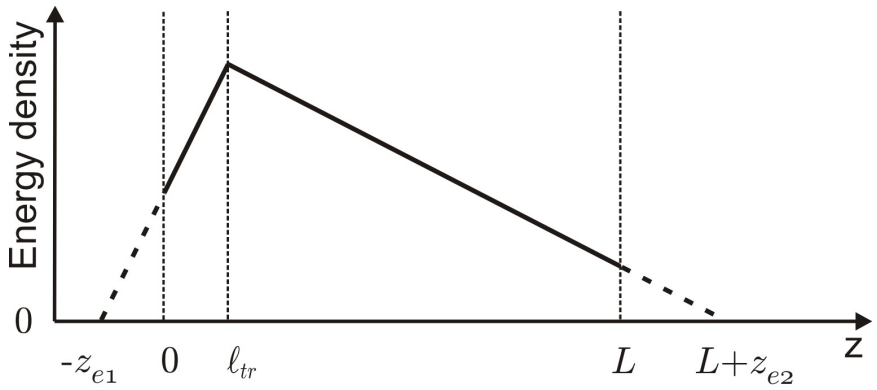


*Figure 2.1: The energy density u as a function of the sample position z. The source is approximated by a plane source of diffusive light at $z = \ell_{tr}$. If the energy density is extrapolated outside the sample, the intensity is zero at $z = -z_{e1}$ and $z = L + z_{e2}$. Image taken from [16]*

function, which is zero for $z < \ell_{\mathrm{tr}}$ and one for $z \geq \ell_{\mathrm{tr}}$. A second integration of the diffusion equation over $z$ leads to:

$$\begin{aligned} u(z) &= K_1 z + K_2, \quad 0 \leq z \leq \ell_{\mathrm{tr}}, \\ u(z) &= (K_1 - \frac{S_0}{D})z + K_3, \quad \ell_{\mathrm{tr}} \leq z \leq \text{Ł}. \end{aligned} \tag{2.17}$$

Two of the three integration constants $K_n$ can be determined by using the boundary conditions Eq. 2.15 and Eq. 2.16. Imposing the condition that the energy densities should be continuous at $\ell_{\mathrm{tr}}$, we find the third integration constant. The solution for $u(z)$ is:

$$\begin{aligned} u(z) &= \frac{S_0}{D}\frac{L - \ell_{\mathrm{tr}} + z_{e2}}{L + z_{e1} + z_{e2}}(z + z_{e1}), \quad 0 \leq z \leq \ell_{\mathrm{tr}}. \\ u(z) &= \frac{S_0}{D}\frac{\ell_{\mathrm{tr}} + z_{e1}}{L + z_{e1} + z_{e2}}(L + z_{e2} - z), \quad \ell_{\mathrm{tr}} \leq z \leq L, \end{aligned} \tag{2.18}$$

This solution is plotted in Fig. 2.1. The maximum energy density is at the source, which is positioned at $z = \ell_{\mathrm{tr}}$. We see that the energy density in the sample decays linear with $z$. If one extrapolates the energy density outside the sample, the energy density is zero at $z = -z_{e1}$ and $z = L + z_{e2}$.

The total transmittance is given by the energy current $J$ directed outward at $z = L$, integrated over the surface of the sample $A$. The total transmittance should be a coefficient independent of the source power, therefore the current is divided by the volume integral over the source $S_0$:

$$T = \frac{\mathbf{J}(L)\mathbf{s}A}{S_0 A} = \frac{\ell_{\mathrm{tr}} + z_{e1}}{L + z_{e1} + z_{e2}}. \tag{2.19}$$

To calculate the total transmittance for an absorbing sample, the diffusion equation needs to be modified. Besides a source, a sink needs to be included. The amount of absorbed light is proportional to the amount of incident light. Moreover light will be absorbed on a characteristic time scale $L_a^2/D$, which is the time after which the light is

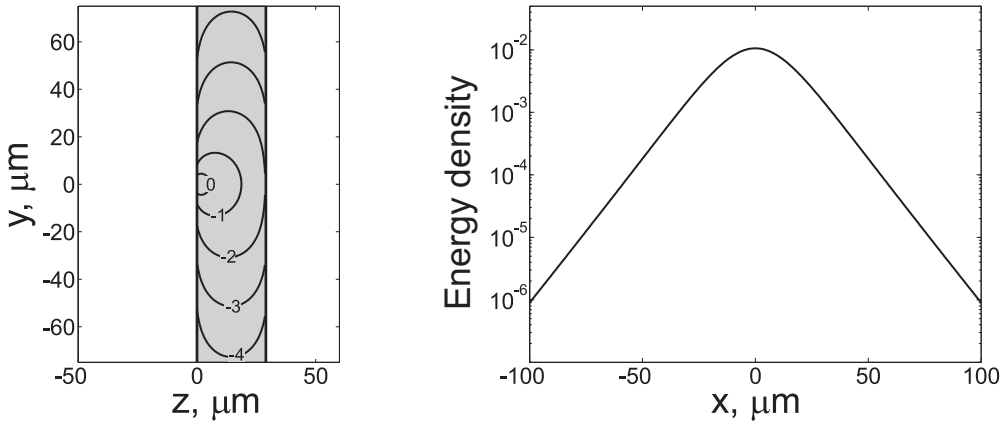


*Figure 2.2: Average distribution of diffusive light in a slab of a strongly scattering material. The sample is 30 μm thick and the source is positioned at z=0.72 μm. On the left hand side a contour plot of the energy density is shown. The contour resembles the log of the energy density* $^{10}\log(u)$*. On the right hand side the intensity distribution at the back of the sample is plotted for the x direction. The results for the y direction are equal. Images are taken from [8].*

attenuated to $1/e$ of the intensity. With absorption, the diffusion equation changes to [17]:

$$-D\nabla^2 u(\mathbf{r},t) = S(\mathbf{r},t) - \frac{L_a^2 u(\mathbf{r},t)}{D}, \tag{2.20}$$

The second term of the right hand side causes the intensity to decay exponentially instead of linearly. The total transmission for an absorbing sample can be found using the Garcia's solution to the diffusion equation [17, 18]:

$$T = \frac{\sinh(\frac{z_p}{L_a}) + \frac{z_{e1}}{L_a}\cosh(\frac{z_p}{L_a})}{(1+\frac{z_{e1}z_{e2}}{L_a^2})\sinh(\frac{L}{L_a}) + \frac{z_{e1}+z_{e2}}{L_a}\cosh(\frac{L}{L_a})}, \tag{2.21}$$

here $z_p$ is the position of the source. As in the non absorbing case we assume that the source to be positioned at $z_p = \ell_{\mathrm{tr}}$. For samples with absorption lengths much larger than both the extrapolation lengths and the transport mean free path, the previous result reduces to:

$$T = \frac{\frac{z_p+z_{e1}}{L_a}}{\sinh(\frac{L}{L_a}) + \frac{z_{e1}+z_{e2}}{L_a}\cosh(\frac{L}{L_a})}. \tag{2.22}$$

If there is no absorption, $L_a$ will be infinite and the expression for an absorbing sample reduces to the previously deduced result for non absorbing samples (Eq. 2.19).

The previous results were deduced for a one dimensional system, now we want to know whether the results are valid for three dimensions too. In literature the solution in three dimensions has been calculated as well, using the boundary conditions in Eq. 2.15 and Eq. 2.16 (see e.g. ref [12]). The solution is plotted in two dimensions in Fig. 2.2. With this solution, the total transmittance can be calculated by integrating the energy current directed outward over the entire surface of the sample. Vellekoop performed this

calculation and showed that the expression for the total transmission in one and three dimensions are identical [19]. From the solution in three dimensions it can also be derived that the radius of the diffusive spot on the back of the sample is comparable to the thickness of the sample [8].

Bret [9] solved the diffusion equation by using an exponential function to describe the light source. The exponential was used because the amount of non diffusive light decays exponentially with $\ell_{\text{tr}}$. In the approximation that the samples have a thickness larger than a few $\ell_{\text{tr}}$, Bret obtained identical results for the total transmission, compared to Eq. 2.19.

In this section we have derived an analytic equation for the diffusive total transmission in a one dimensional slab geometry. The inverse total transmission is linear with the sample thickness. In literature we found that the this solution for the total transmission is also valid for three dimensional slab geometries.

### 2.2.5 Scattering channels and transmission coefficients

This subsection serves to introduce scattering channels (i.e channels) and transmission coefficients. We will use the channels and transmission coefficients to describe the speckle correlation functions and the wavefront shaping experiments.

To describe the electric field at a position $\mathbf{r}_1$ in a random scattering medium one has to consider the Green function $G(\mathbf{r}_1, \mathbf{r}_2)$. The Green function describes the propagation from a source positioned at $\mathbf{r}_2$ to $\mathbf{r}_1$. The problem arises that infinitely many positions $\mathbf{r}_1$ exist. This issue is dealt with by grouping these positions $\mathbf{r}_1$ into discrete channels. The Green function can also be described in angular space, then it describes the propagation from light in at an incident angle to light in another outgoing angle.

In real space the channels are described as a diffraction limited spot of an area in the order of $\lambda^2$ [2]. In angular space the channels can be described as as the waveguide modes of a perfect waveguide. In this approach the evanescent fields are neglected, which is a valid approach because the evanescent fields do not propagate towards a detector in the far field.

The incident light is described by a complete set of channels. The incident and outgoing light (except for the evanescent fields) can always be described as a linear combination of the in and outgoing channels.

The propagation of the electric field from channel $a$ to channel $b$ is described by the complex transmission coefficient $t_{ab}$. Similarly $T_{ab} = |t_{ab}|^2$ is the intensity transmission coefficient [20]. The transmission coefficient depends strongly on the frequency $\omega$. The number of channels for a sample with surface area A is approximately $A/\lambda^2$, where lambda is the wavelength of light.

### 2.2.6 Phase derivatives

The transmission coefficients have been introduced in the previous subsection. We will now study the frequency dependence of these transmission coefficients.

The frequency dependence of a transmission coefficient is described by the phase derivative, which is a quantity closely related to the path lengths inside the random scattering material. The properties of phase delay times can be computed using diffusion theory. Moreover phase delay times can be measured in experiments. The phase delay time is the

phase derivative $\partial\phi/\partial\omega$ of the phase of the complex transmission coefficient $t_{ab}$ [21], i.e. the rate at which the phase changes with respect to frequency changes.

To understand phase delay times, we first consider two different physical paths inside a random scattering medium. Two fields $E_1$ and $E_2$ have traversed along paths $l_1$ and $l_2$ and arrive at the same position. Changing the frequency leads to an intensity change according to:

$$\begin{aligned} I &= \left| E_1 e^{i\frac{l_1\omega}{c}} + E_2 e^{i\frac{l_2\omega}{c}} \right|^2, \\ &= |E_1|^2 + |E_2|^2 + |E_1|\,|E_2| \cos(\frac{(l_1 - l_2)\omega}{c}). \end{aligned} \tag{2.23}$$

The fluctuations depend on the path length difference. For this situation the phase derivative would be $(l_1 - l_2)/c$, where $c$ is the speed of light in vacuum. The difference between path lengths and phase delay times arises from the fact that there will be infinitely many paths between two positions:

$$I = \sum_a^\infty E_a e^{i\frac{l_a\omega}{c}} \sum_{a'}^\infty E^*_{a'} e^{-i\frac{l_{a'}\omega}{c}}. \tag{2.24}$$

If we acknowledge that this is complex number, with a amplitude and phase which is solely dependent of $\omega$, the sum over paths can be rewritten as:

$$\sum_a^\infty E_a e^{i\frac{l_a\omega}{c}} = E(\omega) e^{i\phi(\omega)}. \tag{2.25}$$

The phase $\phi(\omega)$ can be Taylor expanded around $\omega_0$:

$$\phi(\omega) = \sum_{n=0}^\infty \frac{\partial^n \phi}{\partial \omega^n} \frac{(\omega - \omega_0)^n}{n!}. \tag{2.26}$$

The first derivative of the phase can be computed and therefore it is convenient to approximate the phase to first order:

$$\phi(\omega) \approx \phi_0 + \phi' \Delta\omega. \tag{2.27}$$

Where $\phi'$ is the phase derivative $\partial\phi/\partial\omega$, i.e. the phase delay time. This approximation is valid for small $\Delta\omega = \omega - \omega_0$. If Eq. 2.25 and Eq. 2.27 are combined, the sum over paths can be approximated by:

$$\sum_a^\infty E_a e^{i\frac{l_a\omega}{c}} \approx E(\omega) e^{i(\phi_0 + \phi'\Delta\omega)}, \tag{2.28}$$

Unlike paths lengths, phase delay times can be negative, for example due to resonances inside the sample. The average phase delay time $L^2/D$ is related to the average path length $3L^2/\ell_{\mathrm{tr}}$, by the energy velocity.

If we now look at how the intensity behaves as a function of the frequency, we see that $E(\omega)$ determines the fluctuations in the intensity:

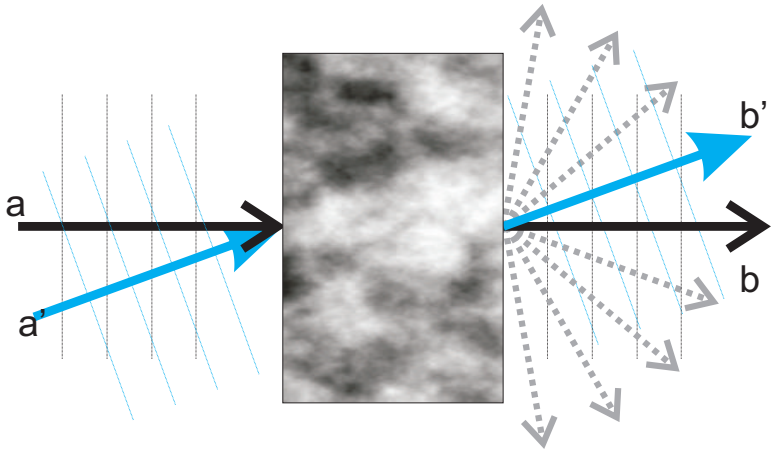


*Figure 2.3: Two ingoing channels $a$ and $a'$, at two different angles. In the random scattering sample these two ingoing channels couple to all outgoing channels, among which the channels $b$ and $b'$. The coupling of the field from $a$ to $b$ and $a'$ to $b'$ is described by transmission coefficients $t_{ab}$ and $t_{a'b'}$.*

$$\begin{aligned} I &\approx \left| E(\omega) e^{i(\phi_0 + \phi' \Delta\omega)} \right|^2 \\ &= E(\omega)^2. \end{aligned} \tag{2.29}$$

## 2.3 Speckle correlation function

In the previous section we have seen that phase delay times describe the frequency dependence of the phase of a transmission coefficient. Because transmission coefficients change gradually when the frequency of the incident light is detuned, correlations among the transmission coefficients will exist. The purpose of this section is to understand and quantify these correlations.

Lee has first shown that intensity transmission coefficients $T_{ab}$ are correlated [22]. Speckle correlation functions are used to calculate and measure these correlations [23]. We will discuss the correlations in angular and frequency space. Two incoming channels are considered, $a$ and $a'$. These channels couple to all the outgoing channels of the sample. Of all outgoing channels we will only consider $b$ and $b'$. All channels have the same frequency $\omega$, which can be detuned to frequency $\omega'$. The channels $a$ and $a'$ differ by a transverse momentum difference $\Delta p_{\perp a}$ and $b$ and $b'$ by $\Delta p_{\perp b}$. The situation is sketched in Fig. 2.3.

The correlation $C_{aba'b'}(\omega, \omega')$ between two transmission coefficients is defined as:

$$C_{aba'b'}(\omega, \omega') = \langle \delta T_{ab}(\omega, \omega') \delta T_{a'b'}(\omega, \omega') \rangle, \tag{2.30}$$

where $\delta T_{ab}(\omega, \omega') = T_{ab}(\omega, \omega') - \langle T_{ab}(\omega, \omega') \rangle$. The brackets $\langle \cdot \rangle$ denote ensemble averaging, i.e. averaging over different realizations of disorder. Berkovits *et al.* have shown that Eq.

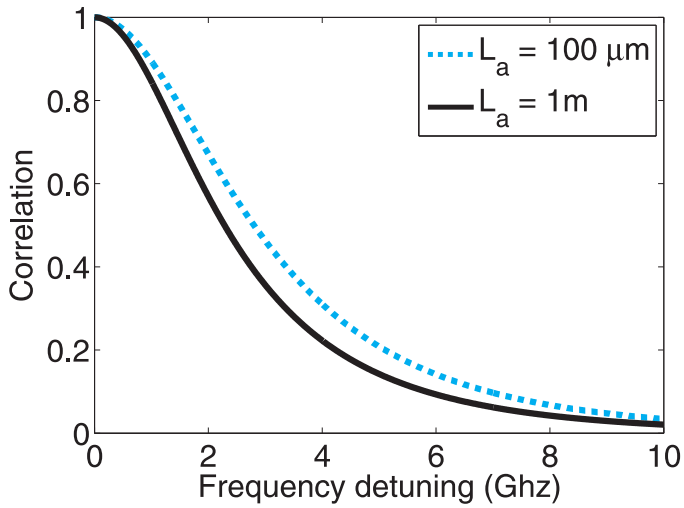


*Figure 2.4: The theoretical prediction of the $C^1$ correlation as a function of the frequency detuning. The sample thickness is 160 µm and the diffusion constant $40\frac{m^2}{s}$. The absorption dependence is shown for $L_a$ equal to 1 m (solid black line) and 100 µm (blue dashed line).*

2.30 can be written as [24]:

$$C_{aba'b'} = |\langle E_{ab} E^*_{a'b'} \rangle|^2 , \tag{2.31}$$

where $E_{ab}$ is the incident field times the amplitude transmission coefficient i.e. $E_a t_{ab}$.

Feng *et al.* [23] have also shown that Eq. 2.30 can be separated into three orders of the conductance $g$, where $g = \sum_{ab} T_{ab} \approx N\ell_{\text{tr}}/L$. The conductance is the sum over all $N$ ingoing and $N$ outgoing channels. A incoming channel has an average transmission $\ell_{\text{tr}}/L$, where $L$ is the sample thickness. Each order of $g$ represents a different kind of correlation, called $C^1$, $C^2$ and $C^3$:

$$C_{aba'b'} = {C^1}_{aba'b'} + {C^2}_{aba'b'} + {C^3}_{aba'b'}, \tag{2.32}$$

where $C^1 \propto 1$, $C^2 \propto g^{-1}$ and $C^3 \propto g^{-2}$. $C^1$ is measured by recording the fluctuations in $T_{ab}$, which means a single ingoing channel is excited and one outgoing channel is measured. The $C^2$ can be measured by considering the fluctuations in total transmission, as a function of one incident channel. The $C^3$ correlations are the optical analog of the Universal Conductance fluctuations [23], which can be measured in an all channels in and all channels out configuration. The total transmission will vary due to a different realizations of disorder, which makes the correlations infinite range. For large $g$, the $C^2$ and $C^3$ correlations can be neglected if one measures the intensity in a one channel in, one channel out configuration. In this work we assume $g \gg 1$ and therefore we neglect $C^2$ and $C^3$ correlations.

Van Rossum [25] has calculated the $C^1_{aba'b'}$ contribution of Eq. 2.32 including absorp-

tion:

$$C^1{}_{aba'b'}(\omega-\omega') = \frac{|M|^2}{\kappa^2}\left|\frac{(1+\kappa^2 z_0^2)\sinh(\kappa L)+2\kappa z_0\cosh\kappa L}{(1+M^2 z_0^2)\sinh(ML)+2Mz_0\cosh ML}\right|^2, \tag{2.33}$$

where $\kappa$ is the inverse absorption length $L_a^{-1}$ and $M^2 = \Delta p_\perp^2 + \kappa^2 + \frac{i\Delta\omega}{D}$. $\Delta p_\perp$ is the perpendicular momentum difference, $z_0$ the extrapolation length and $L$ the sample thickness. In the limit of thick samples (i.e. $L \gg z_0$ and $Mz_0 \ll 1$), this reduces to:

$$C^1{}_{aba'b'}(\omega-\omega') = \frac{|M|^2}{\kappa^2}\left|\frac{\sinh(\kappa L)}{\sinh(ML)}\right|^2. \tag{2.34}$$

If there is no absorption $\kappa$ becomes zero and $\sinh(\kappa L) \approx \kappa L$, thus one obtains:

$$C^1{}_{aba'b'}(\omega-\omega') = \left|\frac{ML}{\sinh(ML)}\right|^2. \tag{2.35}$$

The difference between Eq. 2.33 and Eq. 2.35 is depicted in figure 2.4. To create this picture we assumed that using Eq. 2.33 with an absorption length of 1 m is the same as Eq. 2.33. In the figure we see that both $C^1$ correlation functions are bell shaped, similar to a Gaussian. The frequency width of the $C^1$ correlation is increased due to absorption. If one fits the $C^1$ correlation without absorption to the $C^1$ correlation function with absorption, one will see that the functional form of the $C^1$ correlation function does not change notably due to absorption. For absorption lengths much smaller than the thickness of the sample, large differences will be found between the functional form of $C^1$ with and without absorption.

## 2.4 Frequency correlation with enhanced speckles

In this section we will extend the theory for wavefront shaping experiments to the frequency domain. First we will review the existing theory, which discusses how the intensity in a single channel can be strongly enhanced. Thereafter we will show that the decay of the enhanced speckle intensity due to frequency detuning is described by the $C^1$ correlation. Last, we develop a theory which shows that the frequency width of an enhanced speckle can be controlled.

### 2.4.1 Maximum enhancement

Here we derive an expression for the maximum enhancement of an intensity enhanced speckle. If light is incident in a single channel $a$, the electric field ($E_b$) of an outgoing channel $b$ is determined by the incoming field in the channel $a$ ($E_a$) and the transmission coefficient $t_{ab}$:

$$E_b = t_{ba}E_a. \tag{2.36}$$

The transmission coefficient $t_{ab}$ is a complex quantity of which the amplitude and phase are independently drawn from a circular Gaussian distribution [26], thus $\langle t_{ab}\rangle = 0$.

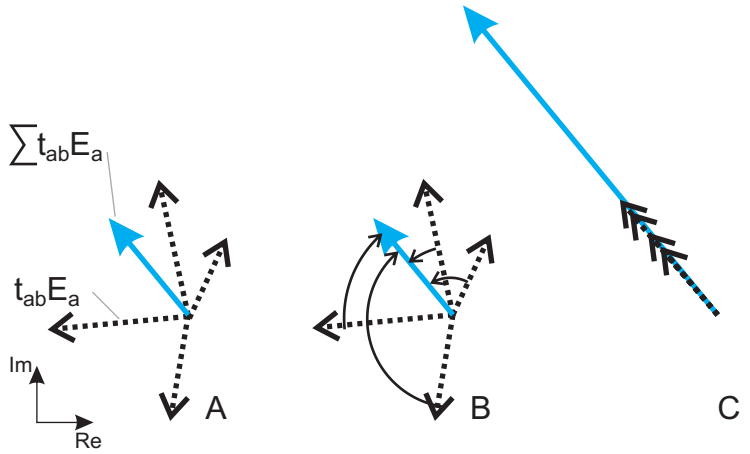


*Figure 2.5: The principle of enhancing the intensity of a speckle. The dashed black arrows represent the complex transmission coefficient times the incoming field $t_{ba}E_a$. At A $t_{ba}E_a$ is random for all $a$, which causes a small resultant vector (solid blue arrow). At B the phase of the incident field $E_a$ is changed such that all the phases of $t_{ba}E_a$ are rotated towards the blue resulting vector. Finally, at C, all the phases are aligned and the resulting vector is strongly increased. For clarity of the picture, the solid blue arrow is not on the same scale as the black arrows.*

For $N$ incoming channels the field is:

$$E_b = \sum_a^N t_{ba} E_a. \tag{2.37}$$

In an experiment amplitude and phase of the incident light $E_a$ can be controlled. We want to find the optimal configuration for both amplitude and phase, such that the intensity in a single outgoing channel is maximal. We will denote this target channel with $\beta$

The intensity in channel $\beta$ is:

$$\begin{aligned} I_\beta &= \left| \sum_a^N t_{a\beta} A_a e^{\phi_a} \right|^2 \\ &= \sum_a^N |t_{a\beta}|^2 A_a^2 + \sum_a^N \sum_{a' \neq a}^N t_{a\beta} A_a e^{\phi_a} t^*_{a'\beta} A_{a'} e^{-\phi'_a} \end{aligned} \tag{2.38}$$

The intensity $I_\beta$ can not be calculated for a single realization of disorder. Therefore we look at the average of $I_\beta$. To calculate the average of $t_{a\beta} A_a e^{\phi_a} t^*_{a'\beta} A_{a'} e^{-\phi'_a}$ we use the statistical properties of this term. We can use the fact that for two independent variables $A$ and $B$, the average of the product is equal to the product of the averages [26]. Since $t_{ab}$ and $t_{a'b}$ are independent of each other and independent of both $A_a e^{\phi_a}$ and $A_{a'} e^{-\phi'_a}$, the

average of the term $t_{a\beta}A_a e^{\phi_a} t^*_{a'\beta}A_{a'}e^{-\phi'_a}$ will be zero. This results in:

$$\langle I_{\beta,0}\rangle = N\langle|t_{a\beta}|^2\rangle\langle A^2\rangle \tag{2.39}$$

A way to make sure that the term $t_{a\beta}A_a e^{\phi_a} t^*_{a'\beta}A_{a'}e^{-\phi'_a}$ does not average out to zero is by making it positive for all $a$ and $a'$. Because $t_{a\beta}A_a e^{\phi_a} t^*_{a'\beta}A_{a'}e^{-\phi'_a}$ is complex, the term will be positive if all phases add up to zero:

$$\phi_a - \phi_{a'} + \arg(t_{a\beta}) - \arg(t_{a'\beta}) = 0 \quad \text{for all } a \tag{2.40}$$

For all $a$ the following solution is found:

$$\phi_a = -\arg(t_{a\beta}) + C, \tag{2.41}$$

where $C$ is a constant independent of $a$. The principle of enhancing a speckle as described in the previous Eq. 2.41 is described graphically in Fig. 2.5. In A we see that the fields in the outgoing channel (black dotted arrows) add randomly, leading to a small field (blue solid arrow). The phases are aligned in B, rotating the black arrows is done by changing the phase of the incident light. The result is shown in C, where we see a strongly enhanced field in the outgoing channel.

Using the solution in Eq. 2.41, the following expression is found for the maximum intensity in channel $\beta$:

$$\begin{aligned} I_{\beta,\max} &= \left|\sum_a^N t_{a\beta}A_a e^{\phi_a}\right|^2 \\ &= \sum_a^N |t_{a\beta}|^2 A_a^2 + \sum_{a,a'\neq a}^N |t_{a\beta}|\, A_a \left|t_{a'\beta}\right| A_{a'}. \end{aligned} \tag{2.42}$$

If we consider $A_a$ to be random variables and independent of either $|t_{a\beta}|$, $\left|t_{a'\beta}\right|$ or $A'_a$, the average of this solution is:

$$\langle I_{\beta,\max}\rangle = N\langle|t_{a\beta}\rangle|^2\rangle\langle A^2\rangle + N(N-1)\langle|t_{a\beta}|\rangle^2\langle A\rangle^2 \tag{2.43}$$

The average enhancement $\langle\eta\rangle$ is defined as the ratio between the average peak intensity of an enhanced speckle and the average peak intensity of an average speckle.

$$\langle\eta\rangle = 1 + (N-1)\frac{\langle|t_{a\beta}|\rangle^2}{\langle|t_{a\beta}|^2\rangle}\frac{\langle A\rangle^2}{\langle A^2\rangle} \tag{2.44}$$

The optimum can be found by maximizing $\langle|t_{a\beta}|\, A_a \left|t_{a'\beta}\right| A_{a'}\rangle$ in Eq. 2.42. A choice has to be made how to treat $A_a$ in the optimization. From an experimental point of view two options exist, of which the first is setting all the $A_a$ equal, the second is relating $A_a$ to $|t_{a\beta}|$.

Setting all $A_a$ equal results in the following expression for the average intensity enhancement:

$$\langle \eta \rangle = 1 + \frac{\langle |t_{a\beta}| \rangle^2}{\langle |t_{a\beta}|^2 \rangle}(N-1). \tag{2.45}$$

Where it can be calculated that $\frac{\langle |t_{a\beta}| \rangle^2}{\langle |t_{a\beta}|^2 \rangle}$ equals $\frac{\pi}{4}$ [16]. We find an optimum in the enhancement if $A_a = A_0 |t_{a\beta}|$, with $A_0$ an arbitrary prefactor. With this solution we find the following expression for the average intensity enhancement:

$$\langle \eta \rangle = \frac{\langle |t_{a\beta}|^4 \rangle}{\langle \left| t_{a\beta}^2 \right|^2 \rangle} + (N-1). \tag{2.46}$$

In the previous derivation we have shown that the optimum phase front is found by setting $A_a e^{\phi_a} = A_0 t_{a\beta}^*$. Experimentally this means that the incident field has to be proportional to complex conjugate of the transmission coefficient.

### 2.4.2 Sensitivity of the enhanced speckle intensity to frequency detuning

Now we will discuss how the intensity of a single enhanced speckle decreases when the frequency of the incident light is detuned by $\Delta\omega$ from $\omega_0$, where the optimization was performed.

To describe the frequency dependence of $\langle I_{\beta,\max} \rangle$ we have to take a closer look at Eq. 2.42. As the frequency of the incident light changes, the transmission coefficients $t_{a\beta}$ change, which is denoted by $t_{a\beta}(\omega_0 + \Delta\omega)$. The relative phases and the amplitude of the incident light are assumed to remain equal, therefore the incident light is described by $A t_{a\beta}^*(\omega_0)$. Using these two observations, the frequency dependence of Eq. 2.42 is given by:

$$I_\beta(\omega_0 + \Delta\omega) = A^2 \left| \sum_a^N t_{\beta a}(\omega_0 + \Delta\omega) t_{\beta a}^*(\omega_0) \right|^2. \tag{2.47}$$

This equation can be rewritten in terms of the average over $t_{\beta a}(\omega_0 + \Delta\omega) t_{\beta a}^*(\omega_0)$:

$$I_\beta(\omega_0 + \Delta\omega) = A^2 \left| N \overline{t_{\beta a}(\omega_0 + \Delta\omega) t_{\beta a}^*(\omega_0)} \right|^2. \tag{2.48}$$

For very large $N$ the average can be replaced by an ensemble average, and we find:

$$I_\beta(\omega_0 + \Delta\omega) = A^2 N^2 \left| \langle t_{\beta a}(\omega_0 + \Delta\omega) t_{\beta a}^*(\omega_0) \rangle \right|^2. \tag{2.49}$$

We see that the term describing the decay of the enhanced speckle is equal to the Eq. 2.31, which is the definition of the correlation function $C_{a\beta a'\beta'}(\omega, \omega')$. If $g = \sum_{ab} T_{ab}$ is large, this correlation function corresponds to the $C^1$ correlation shown in Eq. 2.33.

### 2.4.3 The effect of imperfect modulation

Now we deal with the case where the optimization is not optimal, for example when we can not modulate the amplitude, or due to instabilities in the setup.

In previous work from our group the degree of control was introduced as a factor $\gamma$ [27]. The degree of control is defined as the overlap between the used wavefront and the optimal wavefront. Mathematically the degree of control can be expressed as:

$$\gamma \equiv \sum_a^N (E_a^{\mathrm{Opt},\beta})^* E_a^{\mathrm{Act},\beta}, \tag{2.50}$$

where $(E^{\mathrm{Opt},\beta})^*$ and $E^{\mathrm{Act},\beta}$ are the optimal and the actual fields. Above we have shown that $E_a^{\mathrm{Opt},\beta}$ corresponds with $t_{\beta a}(\omega_0)^*$ times a prefactor. The actual field $E^{\mathrm{Act},\beta}$ can be described as a superposition of $E^{\mathrm{Opt}_a,\beta}$ and an error term $\Delta E_a$ [27]:

$$E_a^{\mathrm{Act},\beta} = \gamma E_a^{\mathrm{Opt},\beta} + \sqrt{1-|\gamma|^2}\Delta E_a. \tag{2.51}$$

Here $E_a^{\mathrm{Opt},\beta}$ and $\Delta E_a$ are orthogonal, i.e. $\sum_a^N E_a^{\mathrm{Opt},\beta}\Delta E_a = 0$, and normalized: $\sum_a^N \left|E_a^{\mathrm{Opt},\beta}\right|^2 = 1$, $\sum_a^N |\Delta E_a|^2 = 1$.

With this expression we can repeat the calculation to determine the frequency dependence of the optimum:

$$I_\beta(\omega_0+\Delta\omega) = A^2 \left| \sum_a^N t_{\beta a}(\omega_0) E_a^{\mathrm{Act},\beta} e^{i\phi'_{\beta a}\Delta\omega} \right|^2. \tag{2.52}$$

If we use Eq. 2.51 we find:

$$I_\beta(\omega_0+\Delta\omega) = A^2 \left| \sum_a^N t_{\beta a}(\omega_0)\gamma E_a^{\mathrm{Opt},\beta} e^{i\phi'_{\beta a}\Delta\omega} + \sum_a^N t_{\beta a}(\omega_0)\sqrt{1-|\gamma|^2}\Delta E_a e^{i\phi'_{\beta a}\Delta\omega} \right|^2. \tag{2.53}$$

The cross terms in this equation will average out to zero due to the orthogonality of $\Delta E_a$ and $t_{\beta a}$. The ensemble average of $\langle I_\beta(\omega_0+\Delta\omega)\rangle$ is:

$$\langle I_\beta(\omega_0+\Delta\omega)\rangle = A^2|\gamma|^2 N(N-1)\left|\langle t_{\beta a}(\omega+\Delta\omega)t^*_{\beta a'}\rangle\right|^2 + (1-|\gamma|^2)N\langle|t_{\beta a}(\omega_0)|^2\rangle. \tag{2.54}$$

In case of large $N$ and large $\gamma$, the second term can be neglected. Assuming $\gamma$ is frequency independent, the frequency behavior of an enhanced speckle will be independent of the degree of control. We see that the average intensity of the enhanced speckle is decreased by a factor $|\gamma|^2$. Thus for any enhanced speckle we expect to find the same average frequency width. For small $\gamma$ or small $N$ the second term in Eq. 2.54 will cause background fluctuations with respect to the $C^1$ correlation. For small $N$ the previously neglected cross terms do not average out anymore.

### 2.4.4 Phase delay time control

We have shown that an enhanced speckle has a similar frequency behavior as the speckle correlation function. We now want to shape the incident wavefront such that a speckle consists of solely small or large phase delay times.

The basic thought is to make the previously discussed error term $\Delta E_a$ frequency dependent. This can be done by creating an enhanced speckle at two different frequencies $\omega_0$ and $\omega_1$ and adding those phase fronts. This results into the following expression:

$$I_\beta(\omega_0 + \Delta\omega) = \left| \sum_a^N t_{\beta a}(\omega_0) A [\frac{1}{2} t^*_{\beta a}(\omega_0) + e^{i\phi} \frac{1}{2} t^*_{\beta a}(\omega_1)] e^{i\phi'_{\beta a} \Delta\omega} \right|^2 , \tag{2.55}$$

where $t^*_{\beta a}(\omega_0)$ is the optimal phase front for frequency $\omega_0$ and $t^*_{\beta a}(\omega_1)$ perfectly matches frequency $\omega_1$. One can choose a phase dependence of $e^{i\phi}$ between both phase fronts. In the rest of this derivation we choose $\phi$ to be zero or $\pi$.

The expression can be expanded into four terms which results in:

$$\begin{aligned} I_\beta(\omega_0 + \Delta\omega) &= \sum_{a,a'}^N \frac{1}{4} A^2 t_{\beta a}(\omega_0) t^*_{\beta a}(\omega_0 + \Delta\omega) t^*_{\beta a'}(\omega_0) t_{\beta a'}(\omega_0 + \Delta\omega) \\ &+ e^{i\phi} \frac{1}{4} A^2 t_{\beta a}(\omega_0) t^*_{\beta a}(\omega_0 + \Delta\omega) t^*_{\beta a'}(\omega_0) t_{\beta a'}(\omega_1 + \Delta\omega) \\ &+ e^{-i\phi} \frac{1}{4} A^2 t_{\beta a}(\omega_0) t^*_{\beta a}(\omega_1 + \Delta\omega) t^*_{\beta a'}(\omega_0) t_{\beta a'}(\omega_0 + \Delta\omega) \\ &+ \frac{1}{4} A^2 t_{\beta a}(\omega_0) t^*_{\beta a}(\omega_1 + \Delta\omega) t^*_{\beta a'}(\omega_0) t_{\beta a'}(\omega_1 + \Delta\omega). \end{aligned} \tag{2.56}$$

The first term is most easy recognizable, since it is exactly Eq. 2.47. The fourth term equals Eq. 2.47 if $\Delta\omega = \omega_0 - \omega_1$, which can be interpreted as a $C^1$ peak shifted from $\Delta\omega = 0$ to $\Delta\omega = \omega 0 - \omega 1$. If $\omega_1$ and $\omega_0$ differ sufficiently, one will see two independent $C^1$ peaks centered at frequencies $\omega_0$ and $\omega_1$.

If we choose $\omega_0 - \omega_1$ sufficiently small the cross terms come into play. These terms are equal to the first term times $e^{i(\omega_1 - \omega_0)\phi'_a}$. One can see that these cross terms are dependent on the phase delay times, and only survive when the product $(\omega_1 - \omega_0)\phi'_a < \frac{\pi}{2}$. We conclude that the cross terms are a handle to select phase delay times which are smaller than a particular magnitude. Now we can, by setting the phase factor $e^{i\phi}$ equal to plus or minus, choose to either subtract or add these small phase delay times, and thus leading to a thinned or widened correlation peak.

## 2.5 Conclusions

We have reviewed the theory on the diffusion of light in random scattering materials which is of interest for this thesis. The existing theory for the creation of enhanced speckles is extended to the frequency domain.

The main new result is a theory we developed showing how the intensity of an enhanced speckle decreases when the frequency of the incident light is detuned. It was shown that

the intensity of an enhanced speckle decays like the $C^1$ correlation function when the frequency of the incident light is detuned. Imperfections in the spatially shaped wavefront which creates the enhanced speckle only influences the intensity of the enhanced speckle, and not the frequency width of the enhanced speckle.

We also developed a theory to show that the frequency width of a enhanced speckle can be controlled. Large phase delay time can be selected, and by either subtracting or adding their contribution to the enhanced intensity, the frequency width of an enhanced speckle can be increased of decreased.

Chapter 3

# Instrumentation

## 3.1 Introduction

We now focus our attention on the instrumentation we used for the experiments in which we first create an enhanced speckle and thereafter detune the frequency of the incident light. The enhanced speckle is created by shaping the incident wavefront. We used the similar apparatus and software as previous wavefront shaping experiments [3, 27–29]. To detune the frequency, a monochromatic laser is used of which the frequency can be finely detuned. The laser frequency is calibrated using the well documented absolute frequencies of the Cesium resonances.

We first present an overview of the setup in Section 3.2. The laser and the calibration of the frequency scan are discussed in Section 3.3. In Section 3.4 we focus on the performance of the wavefront shaping. We demonstrate full control over the phase and amplitude of the incident light and we characterize the intensity enhancements we are able to obtain with our setup.

## 3.2 Setup

The setup we used for all our experiments is now discussed. The setup is presented in Fig. 3.1. Three different parts can be distinguished. First, the core of the setup is the wavefront shaping. Second, we image the transmitted light on a detector. Last, a part of the setup is used to calibrate the laser frequency.

The 852 nm laser light is coupled into a single mode fiber. The advantage of the light emitted from the fiber is that it does not move in space, opposed the to the light emitted

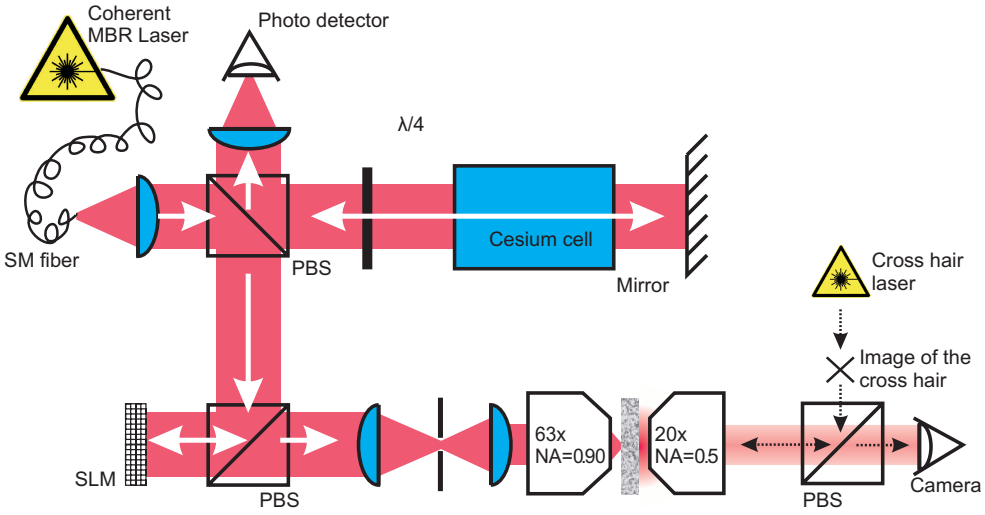


*Figure 3.1: Experimental setup. The light emitted by a Coherent MBR-110 laser is coupled into a single mode (SM) fiber. The divergent light coming out of the fiber is collimated by a lens and split into two orthogonal polarizations by a polarizing beam splitter (PBS). The p-polarized light is used for saturated spectroscopy, where the $\lambda/4$ waveplate ensures that the light which has traveled through the Cesium cell ends up at the photo detector. The s-polarized light is directed towards the SLM. Using the SLM, a 2:1 demagnifying telescope and a pinhole we spatially modulate the phase and amplitude. The shaped wavefront is focussed by the first microscope objective onto the sample. The light transmitted through the sample is imaged on a detector by the second microscope objective, at 160 mm from the microscope objective. A cross hair laser images a cross hair at a distance of 160 mm of the microscope objective. The light emitted by the cross hair laser is focussed on the sample and partially reflected by the sample. A cross hair is imaged on the camera if the camera is at 160 mm from the microscope objective and if the sample is in focus of the microscope objective.*

by the laser. The light is randomly polarized by the fiber and split by a polarizing beam splitter cube (PBS). The light coupled out of the fiber is collimated with a lens. One polarization is sent to the part of the setup which calibrates the laser frequency, and the other is used for wavefront shaping.

To shape the wavefront, the s-polarized beam which is reflected by the PBS is projected on a Spatial Light Modulator (SLM). Each pixel of the SLM independently introduces a phase delay and rotates the polarization of the light. Using the SLM, a PBS, a 2:1 demagnifying telescope and a pinhole, we modulate the amplitude and phase of the wavefront. An infinity corrected Zeiss microscope objective (NA=0.90, 63x) focusses the shaped wavefront on the sample.

To detect the light, a Melles Griot microscope objective (NA 0.5, 20x) images one polarization of the transmitted light on a camera. The camera is positioned at 160 mm from the microscope objective, which has a resolution of 1.0 $\mu$m at a wavelength of 852 nm.

To properly allign the microscope objectives they are placed on XYZ stages. The objectives are first placed in each other's focus to ensure the correct relative X and Y position. Then they are moved in Z-direction such that the sample can be placed in between the

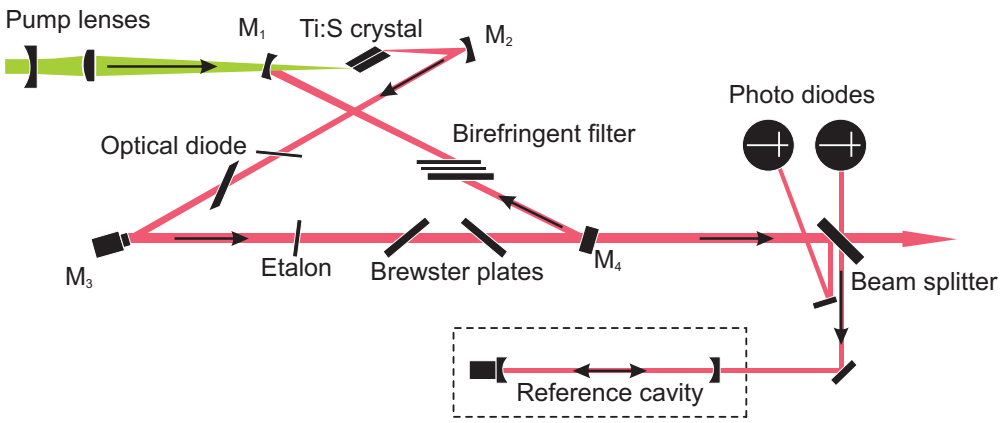


*Figure 3.2: Sketch of the Coherent MBR-110 laser. The laser is used as prescribed by the manual. The pump beam is focussed on the Ti:S crystal. The light emitted by the crystal is blocked in one propagation direction by the optical diode. The birefringent filter is used to determine the coarse center wavelength, the etalon is used for to choose the exact center wavelength. The brewster plates change the effective cavity length to perform the scan. The light emitted by the laser is partially coupled into a reference cavity. Image taken from [30]*

microscope objectives. The sample is placed in the focus of the first microscope objective by examining the beam reflected by the sample back through the microscope objective. When the sample is in the focus of the objective, the reflected beam is collimated.

The Melles Griot microscope objective at the back of the sample has to image the surface on the camera. We use a cross hair laser to align the microscope objective in Z-direction. This laser projects a sharp cross hair in the back focal place at a distance of 160 mm from the microscope objective. The light is directed towards the microscope objective using a PBC. The microscope objective focusses the cross hair laser light onto the sample, and the sample reflects the light partially. The reflected light now follows the same path as the light from the MBR which is transmitted through the sample. A sharp cross hair is imaged on the camera if the camera is at 160 mm from the microscope objective and if the sample is exactly in the image plane of the microscope objective.

To calibrate the laser the light is sent back and forth through a Cesium cell and a $\lambda/4$ wave plate. The wave plate ensures that the light reflects of the PBS and onto a detector. With this setup we can accurately determine position of the Cesium resonances.

## 3.3 Scanning the laser frequency

In our experiments we will scan the laser frequency. We use the Coherent MBR 110 laser for this purpose. The laser has a scan range of 40 GHz [30] and its center wavelength can be chosen between 700 and 970 nm. The specified power is 1 W. The laser is operated as prescribed by the manufacturer.

There are a few important components in the laser namely: the Titania:Saphhire (Ti:S) crystal, the optical diode, the birefringent filter, the brewster plates and the etalon. These components are seen in Fig. 3.2, where we see the setup of the laser. The Ti:S crystal

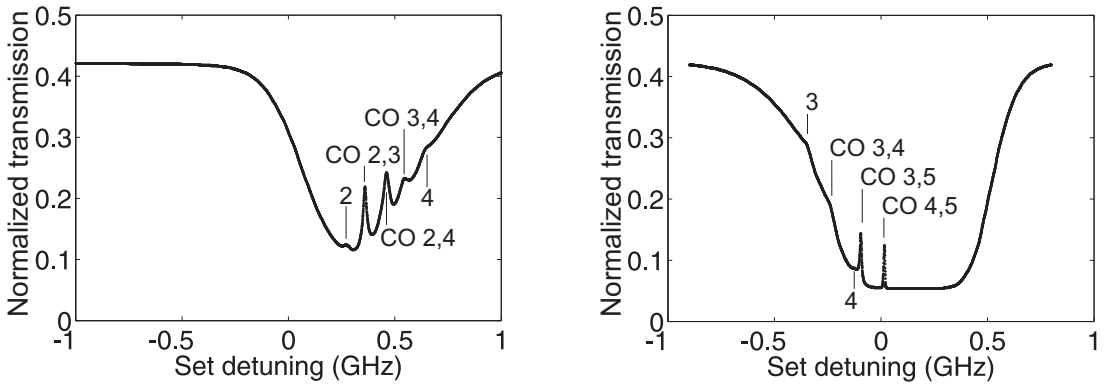


*(a)* *(b)*

*Figure 3.3: The measured resonances of the $D_2$ Cesium spectrum. The transitions from the F=3 ground state in (a), and the F=4 ground state in (b). The crossovers and pure lines are identified using the data of Schmidt [31]. The names indicate what resonance is found, the numbers indicate pure lines and CO a,b indicates a crossover between two pure lines a and b. (a) All expected transitions from the ground state F=3 are present, except for the transition to F'=3. (b) The transitions from the ground state F=4 are also measured, except for the transition towards F'=5.*

is pumped with 8 W, at 532 nm. The emitted radiation can propagate in two directions inside the laser, the optical diode blocks one direction. The birefringent filter selects a small wavelength range of one nanometer. The etalon selects a single cavity mode in this range, which determines the central wavelength at which the scan will start. By rotating the brewster plates, the effective cavity length is changed and as a consequence the laser frequency is scanned.

The cavity has several resonant modes in which light can propagate. During a scan we have to make sure the laser does not hop from one mode to another. If a mode hop occurs, the frequency of the laser will change. To detect this change in frequency a reference cavity is build into the laser. The signal of the reference cavity allows us to determine whether the scan is performed linear with the input voltage [30]. The reference cavity signal is measured and stored for every scan.

The absolute frequency detuning is not given by the set scan width. To determine the absolute frequency we measure the Cesium $D_2$ resonances at 852 nm. The spacing of these cesium resonances is fixed by precision spectroscopy [31]. The resonances are measured in a saturated spectroscopy experiment.

Saturated atomic absorption spectroscopy [32] allows frequency measurements well below the Doppler broadened linewidth, which is over 1 GHz in Cesium [33]. The essence is to use a double pass configuration. Atoms which are resonant with both the beams will experience a higher intensity, therefore be more saturated and absorb less radiation. This can happen in two cases: if the atoms are at rest, or if the atoms move at a specific velocity that makes them resonant with two different Doppler shifted transitions. The first case is called a pure line and the second a cross over (CO).

The result of the saturated spectroscopy experiments is shown in Fig. 3.3, where we plot transitions from the F=3 and F=4 ground states. The transmission of light through a Cesium cell is shown. Small peaks are shown in a larger trough, these peaks can be matched with the lines in theory. In the plot the various peaks are given particular labels which correspond to measured data by Schmidt *et al.* [31].

For both ground states six transitions are expected, where we observe five transitions for each ground state. For the F=3 ground state we expect the transitions to the crossover 2,4 and the pure line F'=3 to be at a distance of 25 MHz. The difference between these two lines could not be resolved, but we know that the peak labeled as CO 2,4 has to be either this cross over or the pure line F'=3. For the F=4 ground state we are able to distinguish the pure line F'=4 and CO 3,5, which are the only transitions spaced by 25 MHz. This knowledge enabled us to identify the other peaks and conclude that the F'=5 transition is absent in our measured spectrum.

The reference cavity ensures a linear scan of the laser frequency, which enables us to calibrate the scan width of the laser with the transitions from F=3 to CO 2,3 and the from F=4 to CO 4,5. The absolute frequency of the scan can be determined with only one of these peaks. The scan width can be calibrated with 20 MHz accuracy and the absolute frequency with 10 MHz accuracy.

## 3.4 Wavefront shaping

In this section we show how the wavefront is shaped such that an enhanced speckle is created. In previous work of our group a new method for wavefront shaping has recently been developed [29], which enables us to modulate amplitude and phase independently, we first introduce this technique. We then show the tests demonstrated earlier by Van Putten *et al.* to ensure that we modulate phase and amplitude independently with our setup. Hereafter we show whether we are capable of creating enhanced speckles and whether the enhancement is in accordance with theory.

### 3.4.1 Four pixel technique

The recently developed four pixel technique is now briefly explained, for a thorough introduction we refer to [29]. With this technique four neighboring pixels are combined into a macropixel. The phase and amplitude of this macropixel can be modulated independently.

The principle of the four pixel method is shown in Fig. 3.4. On the left hand side we see the part of our setup in which the wavefront shaping is performed. The Spatial Light Modulator (SLM) changes the phase and polarization of the incident light as a function of the set voltage on the pixel. By using a Polarizing Beam Splitter (PBS) the polarization modulation is changed into an amplitude modulation. The first diffraction order of the light reflected from the SLM is selected using a pinhole. This means that two neighboring pixels have a phase difference of $\pi/2$. The phase difference of the neighboring pixels is illustrated by the magnified picture of the four pixels. These four neighboring pixels form a so-called macropixel.

The modulation curves of the four pixels are shown in the right hand side illustration. These modulation curves indicate how the phase and amplitude of the light changes when

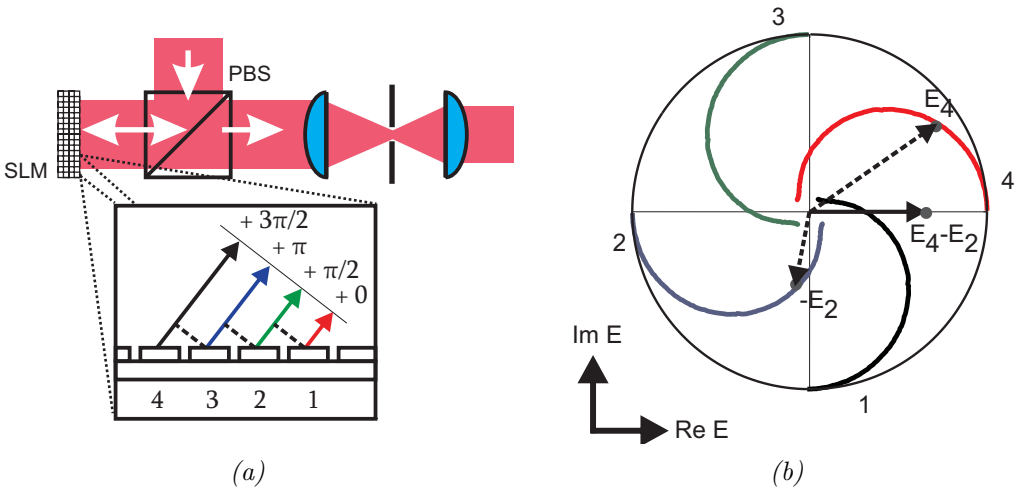


*Figure 3.4: Illustration of the four pixel technique (a) The part of our setup which performs the wavefront shaping. The Spatial Light Modulator (SLM) alters the phase and polarization of the light. The polarization modulation is transformed into an amplitude modulation by the Polarizing Beam Splitter (PBS) The first diffraction order is selected and therefore two neighboring pictures have a phase difference of $\pi/2$ (b) The modulation curves of the four pixels shown in (a). The modulation curve shows how the amplitude and phase of the light change when a voltage is applied to a pixel on the SLM. By choosing the proper voltage of two pixels with a phase difference of $\pi$, the phase or amplitude can be modulated. The example of $E_2$ and $E_4$ illustrates amplitude modulation, the combined fields lead to a solely amplitude modulated macropixel. Pictures taken from [29]*

a voltage is applied on a pixel of the SLM. The modulation curves of the four pixels have a phase difference of $\pi/2$ as shown in the left hand side picture. By combining pixels which have a phase difference of $\pi$, either the phase or amplitude of the light can be controlled by choosing the correct voltage for both pixels. Combining two pixels is shown in the figure, where fields $E_2$ and $E_4$ are combined to create a field with a phase of zero. We have calibrated the SLM such that we know what voltage has to be set on each of the four pixels of a macropixel to create a phase and amplitude modulated wavefront.

### 3.4.2 Independent phase and amplitude modulation

We will now show the measurements from which we can conclude if we have independent phase and amplitude modulation. In the first experiment the phase and amplitude on the entire wavefront are the same. If we use a normal lens to focus a flat wavefront and change the set phase, the measured intensity of the focus should not change if the phase is modulated independent of the intensity.

In Fig. 3.5(a) the measured electric field (actually the square root of the measured intensity) in the focus is plotted as a function of the phase of the shaped wavefront. The amplitude was set to 0.25, 0.5, 0.75 and 1. Ideally the result would be four circles in the complex plane. The measured data lies within 10 % of these circles, which shows that the amplitude remains the same within 10 % as a function of the set phase.

The results in Fig. 3.5(a) do not guarantee that the phase was indeed scanned. If

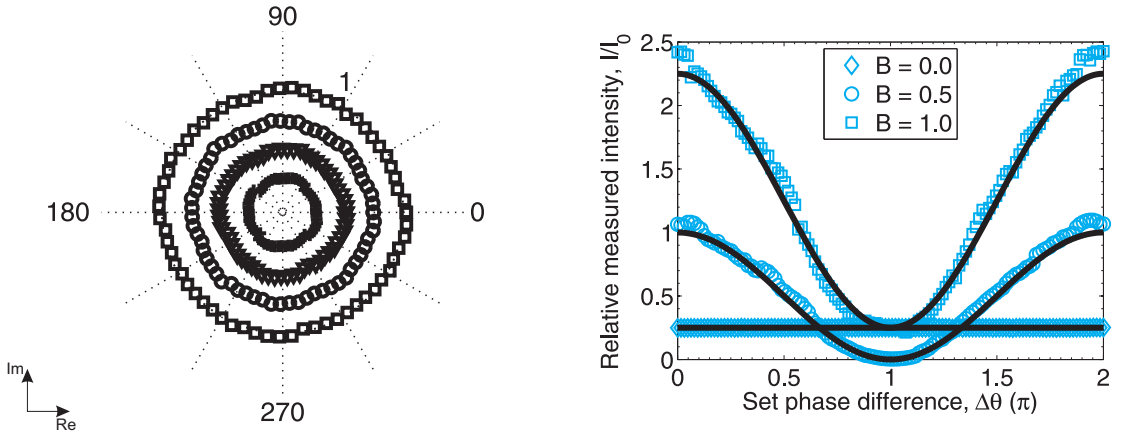


*(a)* *(b)*

*Figure 3.5: Demonstration of independent phase and amplitude modulation (a) The measured amplitude of the focus of a shaped wavefront does not change when the phase of the wavefront is tuned. The experiment is performed for amplitudes 0.25, 0.5, 0.75, and 1. (b) The zero$^{th}$ order of a diffraction pattern generated by a wavefront with rules and notches depends on the phase difference between the rules and notches. The rules and notches have amplitudes of A and B respectively. In this experiment A is set to 0.5 and B to 0, 0.5 and 1. For B equal to 0.5 and 1 we expect the sinusoidal behavior seen in this plot.*

the shaped wavefront is a grating, the influence of the actual phase can be measured. We construct a grating which has rules and notches with amplitudes $A$ and $B$, and a phase difference $\Delta\theta$. If we focus the light modulated by the grating, a diffraction pattern will be detected of which the zero$^{\text{th}}$ order has an intensity depending on the phase difference $\Delta\theta$. [16]:

$$I = A^2 + B^2 + 2AB\cos(\Delta\theta) \tag{3.1}$$

In the experiment we performed, we choose $A$ to be 0.5, and set $B$ to 0, 0.5 and 1. In Fig. 3.5(b) we present the measured intensity as a function of $\Delta\theta$ for the three values of $B$. We see the expected sinusoidal behavior if $B$ is 0.5 or 1, if $B$ is set to zero we see the expected constant intensity. The measured intensity is divided by a constant prefactor to compare the data to Eq. 3.1. We conclude that there is a good correspondence between experiment and theory. From both plots in Fig. 3.5 we conclude that phase and amplitude are modulated independently in our setup within 10 % accuracy.

### 3.4.3 Creating enhanced speckles

With the independent phase and amplitude modulation we should be able to create an enhanced speckle. We will work with a much thicker sample, 155 $\mu$m, than used before and therefore creating an enhanced speckle is not trivial. We will now first show whether an enhanced speckle can be created, and thereafter the results of 81 enhancements are shown and we study the statistics.

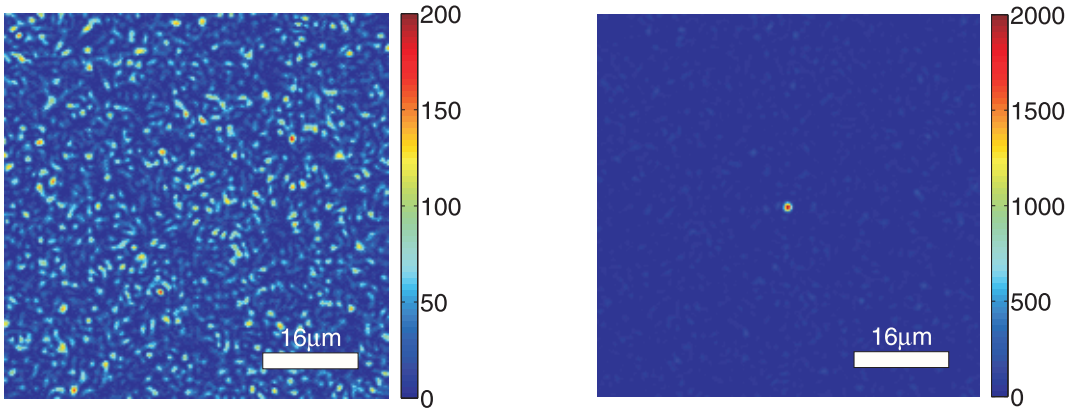


*(a)* *(b)*

*Figure 3.6: (a) The speckle pattern before shaping the wavefront (b) An enhanced speckle we created on a 155 $\mu$m thick sample with our apparatus.*

In Fig. 3.6 we see a typical speckle pattern on the left, where the phase and amplitude of the light are randomly shaped. As shown on the right hand side of Fig. 3.6, the intensity in a single speckle was strongly enhanced after running a stepwise sequential algorithm [34] three times. We see that the enhanced speckle is three to five pixels in diameter, which is 22±5 $\mu$m. This diameter is expected from our microscope objective which has resolution of 1 $\mu$m and a 20 times magnification.

From this measurement we can conclude that we are able to create a focus behind a sample which is 155 $\mu$m thick. In Chapter 4 we will see that the sample is around 200 transport mean free paths thick. The samples previously used are in the order of 40 transport mean free paths thick [27].

The modulated wavefront consists of 208 segments, these segments consist of a number of macropixels. We tried to use 1000 segments, but in these experiments we were limited by the instability of the setup and therefore we did not obtain high enhancements. The phase and amplitude of each segment is modulated. The contribution of a segment to the enhanced speckle is measured in the experiment and is determined by the transmission coefficient the segment couples to. The average contribution of a segment is determined by the amplitude of the incident light, the transmission of the optics and the efficiency of the wavefront modulator.

In Fig. 3.7(a) the average amplitude of each segment on the wavefront is shown. The segments in the corners are set to zero amplitude. We see a distribution in amplitudes, which is caused by the intensity profile of the incident beam. In Chapter 2 it was shown that for a distribution in the amplitudes the enhancement is given by Eq. 2.44. Using this equation, we calculated an expected average enhancement of 149 , where we used the distribution of amplitudes in Fig. 3.7(a).

A histogram with all the measured enhancements is shown in Fig. 3.7(b). We see that the most frequent enhancement is in the bin at an enhancement of 140. Enhancements between 110 and 180 are found. The full width at half maximum of the distribution is 20.

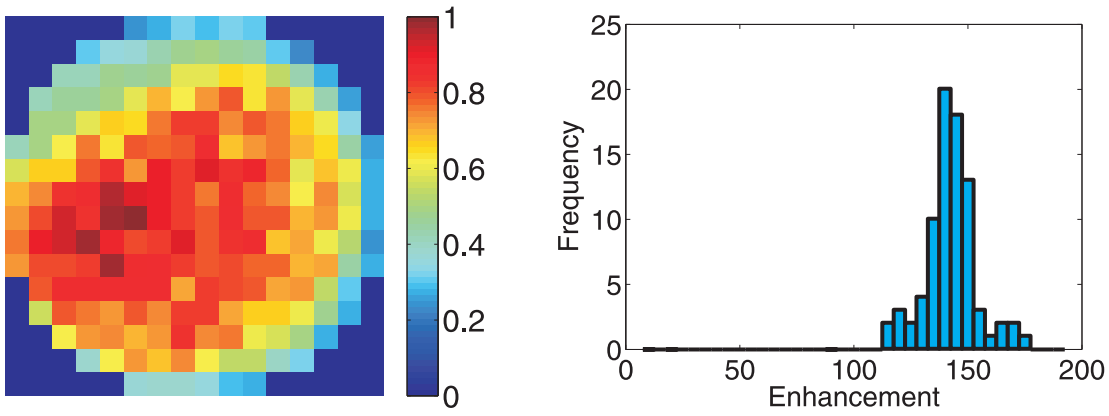


*(a)* *(b)*

*Figure 3.7: (a) The average amplitude of each segment. There is a distribution in the amplitudes because waist of the incident beam is in the order of the height of the SLM. (b) The histogram of the 81 enhancements of different optimizations, on different sample positions. The obtained enhancements are close to the theoretically expected mean value of 149.*

The average enhancement of this distribution is calculated to be 143. This is very close to the predicted enhancement of 149.

## 3.5 Conclusions

We have build a setup which combines a tuneable laser with a wavefront shaping setup. To calibrate the scanning laser a saturation spectroscopy setup is built. In this chapter the resonances in the Cesium spectrum were identified at 852 nm. With the Cesium spectrum we can calibrate the laser frequency with 10 MHz accuracy, and the scan width with 20 MHz accuracy. We showed that we can control the phase and amplitude of the wavefront independently. By shaping the incident light we were capable of creating enhanced speckles near the theoretically expected maximum. These enhancements are obtained in a sample of 200 transport mean free paths thick, which is five times thicker than demonstrated before.

Chapter 4

# Sample fabrication and characterization

## 4.1 Introduction

In our experiments we want to measure the intensity of an enhanced speckle when the frequency of the incident light is detuned. The samples we do experiments on are strongly scattering. To create these samples we typically use structures of randomly ordered nanoparticles. The particles will scatter stronger if the refractive index is large with respect to the medium they are in. For this reason materials like gallium phosphide and titanium dioxide are often used. Another important aspect of the samples is that they should not absorb.

For our experiments the scan range of the laser imposes extra requirements on the samples we can use. The purpose of this chapter is to show how the sample requirements are met, and what the characteristic properties of the samples are. In this chapter we first discuss what the requirements on the samples are. We then discuss how the samples are produced, and how this procedure could influence the properties of sample. We conclude with an analysis of the sample structure and the optical properties.

## 4.2 Sample requirements

The frequency width of the $C^1$ correlation function scales with the diffusion constant $D$ and the sample thickness $L$ as $\Delta\omega = D/L^2$. In order to resolve the $C^1$ correlation, $\Delta\omega = D/L^2$ should be smaller than the scan range of the laser. The maximum scan range of our laser is 40 GHz, therefore we impose the requirement that $\Delta\omega = D/L^2 < 40$ GHz.

To estimate the required sample thickness we look at the well characterized zinc oxide (ZnO) samples. These samples are expected to have a $\Delta\omega = D/L^2$ in the order of 0.5 THz [8]. If we are able to create samples with a comparable diffusion constant, they should be approximately three times the thickness of the previously fabricated ZnO samples, which is around 100 $\mu$m.

## 4.3 Sample fabrication

In this section the fabrication procedure is explained. We intended to follow a recently introduced sample fabrication method, in which an airbrush is used to create a layer of paint [16]. With this method we did not obtain the required thicknesses. Therefore we have chosen to fabricate the sample by deposition of the paint with a pipet. This technique leads to the required sample thicknesses. We first introduce the issues with the airbrush technique and then discuss the fabrication procedure using a pipet.

### 4.3.1 Sample preparation using an airbrush

We intended to create samples by air brushing a suspension of $TiO_2$ particles and water on a microscope cover slide. This deposition technique creates layers in which the scattering particles are homogenously spread in the layer [16].

First a suspension of $TiO_2$ particles in water and binder [35] is created and homogenized by using a rollerbank for thirty minutes. The suspension was placed in an ultrasonic bath for five minutes to separate clustered particles. The substrates, 160 $\mu$m thick cover glasses, were rinsed with subsequently acetone, isopropanol and water, and were left to dry. While airbrushing the suspension on the substrate, the newly deposited suspension pushed the deposited suspension of the glass plate. This effect caused the layer thickness to be limited to a maximum of 50 $\mu$m. Moreover the samples have a granular surface and are quite brittle.

We tried to prevent the suspension flowing away by making the suspension more viscous. We varied the amount of particles [36, 37]. Unfortunately with viscous suspensions, the air brush starts to clog and suspension is sputtered out instead of flowing. The sputtering caused large thickness fluctuations of the sample.

The problem of the suspensions flowing away could also be solved by mixing the $TiO_2$ [36, 37] with ethanol. Because the ethanol evaporates rapidly, the suspension does not flow of the glass plate. Moreover the suspension flows easily through the airbrush, and clogging is prevented. However, the particles in the samples produced this way did not bond sufficiently and therefore the layer falls apart when it is dry.

### 4.3.2 Sample preparation using a pipet

Because the Airbrush method was not working as expected, we tried a new method. The samples used in the optical experiments are prepared by depositing droplets of paint on a cover glass. The sample preparation can be separated into three steps; first cleaning the substrate, then preparing the paint and third the deposition of the paint.

We used commercial paint [35] consisting of $TiO_2$ particles, water and acrylic copolymer as a binder. The paint was used as delivered by the manufacturer. The particles

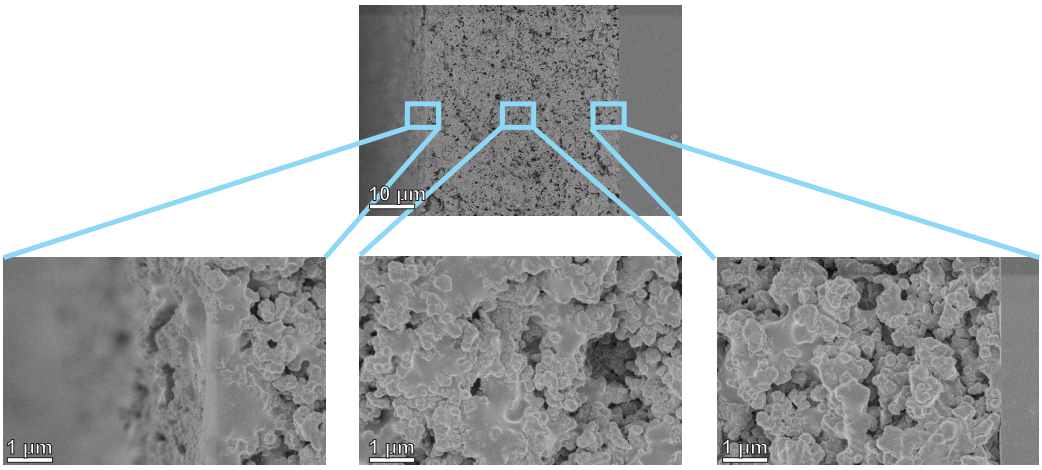


*Figure 4.1: Scanning Electron Microscope (SEM) picture of the cross section of a thin sample ($40\pm3\,\mu$m) of commercial paint ($TiO_2$). The paint is deposited on a glass plate using a pipet. The top picture shows the entire cross section, the glass plate is on the right, on the left we see the paint-air interface. The blue rectangles show where the magnified pictures are taken. As far as can be seen by eye, the particle distribution is homogenous*

precipitate if the paint is not used for some time. Therefore the paint is homogenized by stirring it on a rollerbank for at least half an hour. Clustered particles are separated by putting the paint in an ultrasonic bath for five minutes.

For these samples we used the same microscope cover glasses as in the airbrush experiments. The cleaning of these substrates was performed the same as in the experiments with the airbrush. The paint is put on a microscope cover glass using a pipet. We prepared different samples by depositing different amounts of paint. Droplets ranging from 10 $\mu$l to 100 $\mu$l were deposited on the substrate. The pipet was moved around the glass plate during the deposition of the paint which made sure the paint was well spread on the substrate. We left the samples to dry in a fume hood for a day.

After drying the samples, they were inspected by eye and the optical microscope. In some samples cracks were found, these samples are not used for further experiments. The thickness of the samples was measured using an optical microscope. The varied droplet size has lead to samples thicknesses in the range from 38 $\mu$m to 155 $\mu$m. The sample have thickness fluctuations in the order of five to ten micrometers, but the thickness changes very gradually.

## 4.4 Sample characterization

To see whether our samples match our requirements, we have to characterize the samples. Both the structural and optical properties are analyzed. To see whether the particles are homogenously spread in the layer, we made Scanning Electron Microscope (SEM) pictures of thickest and thinnest samples. The optical properties are determined by measuring the total transmission as a function of sample thickness.

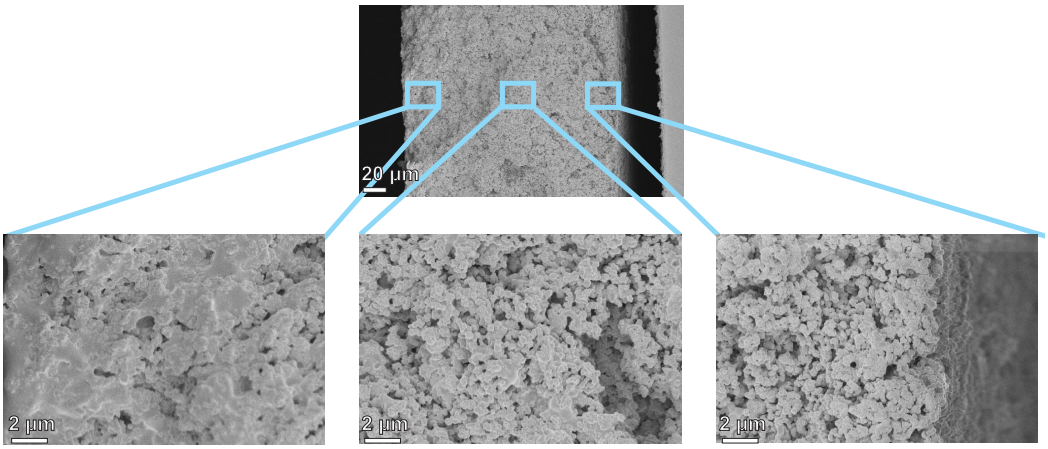


*Figure 4.2: Scanning Electron Microscope (SEM) picture of the cross section of a thick (141±13 µm) sample of commercial paint. The paint is deposited on a glass plate using a pipet. The top picture shows the entire cross section which is made by breaking the sample, which caused the layer of paint to be released of the glass plate. From left to right we see: air, paint, air and glass. The blue rectangles show where the magnified pictures are taken. On the picture in the lower left corner we see a large amount of co-polymer.*

### 4.4.1 Sample structure

We want to see whether the $TiO_2$ particles are homogenously spread in the layers of paint. Because thick sample take longer to dry, we will compare thin and thick samples. We analyzed these samples using SEM images. In Fig. 4.1 the cross section of a thin sample is shown (40±3 $\mu$m). The cross section was made by breaking the sample. The top picture is an overview of the entire cross section. On the right side one can see the glass. In the middle we see the layer of paint and on the left side the interface between the paint layer and air.

The bottom row of Fig. 4.1 shows magnified images of the cross section. On these pictures the individual particles can be distinguished. Through the entire layer one can see clutters of the co-polymer which binds the particles. It is not excluded that the individual particles are $TiO_2$ particles covered in co-polymer. The distribution of particles appears homogenous, albeit the top (left hand side in the picture) micrometer appears to be covered with co-polymer.

The cross section of the thick (141±13 $\mu$m) sample is shown in Fig. 4.2. While breaking the sample, the paint lost contact with the glass at the fracture. The top picture therefore shows, from left to right, the glass, air, paint and air. If one analyzes the pictures at a larger magnification, one can see that the amount of co-polymer increases significant as one moves from the glass plate to the sample surface. It is plausible that the evaporating water transports the co-polymer across the layer. If the drying process is not uniform across the layer, high concentration differences in the co-polymer can be found.

The picture on the right hand of the bottom row has a low concentration of co-polymer, which allows us to determine the particles size of the paint. For this picture the average particle diameter is 0.22 $\mu$m, and the standard deviation is 0.07 $\mu$m.

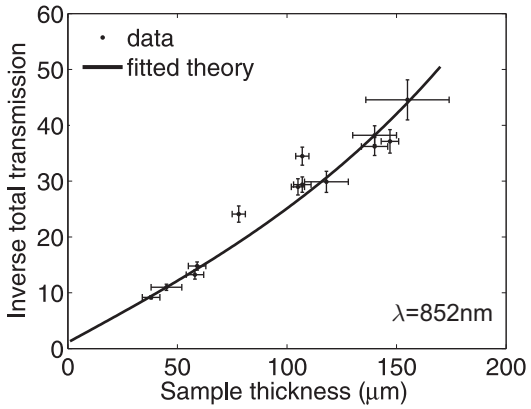


*Figure 4.3: The inverse total transmission measured as a function of the sample thickness at a wavelength of 852 nm. These samples are not entirely flat which causes an error in the thickness. The error in the inverse total transmission is caused by noise. The data is fitted with the theory for absorbing slab geometries.*

From the analysis of SEM images of the thickest and thinnest samples, we have found that the co-polymer is spread inhomogeneously in the thick sample. This may cause the effective refractive index and therefore also the diffusion constant of the sample to be slightly inhomogeneous. We found a particle size of $0.22 \pm 0.07\,\mu$m.

### 4.4.2 Optical properties

We want to characterize the sample such that we can estimate the diffusion constant $D$ and the fluctuations in the diffusion constant. To determine the diffusion constant, we need the transport mean free path $\ell_{\rm tr}$ and the energy velocity $v_{\rm e}$. We will first show how the transport mean fee path and the energy velocity can be extracted from total transmission, and then we present our results.

In the field of strongly scattering materials, total transmission experiments are performed to determine the transport mean free path of samples. The effective refractive index can also be obtained from total transmission experiments [16]. Calculations were used to determine the reflection coefficients in the extrapolation lengths in Eq. 2.15. With these calculations the total transmission is expressed as a function of the transport mean free path, the effective refractive index and the sample thickness.

Samples were made in a thickness range from $5\,\mu$m to $35\,\mu$m, and their total transmission was measured. The inverse total transmission is plotted as a function of sample thickness and then the theory for the total transmission is fitted to the data. From the fit $\ell_{\rm tr}$ and $n_{\rm eff}$ are extracted. This approach has been applied to the samples made from ZnO nanoparticles in air. For these samples it was found that $n_{\rm eff} = 1.4$ and $\ell_{\rm tr}$=0.72 $\mu$m at a wavelength of 532 nm. [16]

We performed the total transmission experiments as described in various works (see e.g. [16, 19]). These experiments are usually performed with a monochromatic light source. The light is focussed on the sample and the transmitted light is collected by an

integrating sphere, which is a sphere with a scattering coating in the inside such that it scrambles the light emitted at various angles. A detector in the sphere detects the light, this signal is interpreted as the transmission averaged over all angles. We used a Fianium super continuum white light source of which the wavelengths below 500 nm were filtered instead of a monochromatic laser source. This light source enables us to measure $\ell_{\text{tr}}$ for an entire spectrum with a spectrometer. The spectrum has a good signal to noise ratio between 500 and 900 nm.

Before we analyze the entire spectra obtained with the Fianum, we first consider the total transmission at a wavelength of 852 nm. At this wavelength we performed the experiments in Chapter 5. In Fig. 4.3 we show the inverse total transmission as a function of thickness at a wavelength of 852 nm. We see that the inverse total transmission does not increase linearly with the sample thickness, which implies the sample absorbs. We fitted Eq. 2.21 to the data, which takes absorption into account. The figure shows that a reasonable fit is obtained.

The error in the inverse total transmission is caused by detector noise. The noise can be estimated by determining the standard deviation of the values in the range from 850 nm to 854 nm. We use two times the standard deviation as the error. The error of the sample thickness is a few micrometers, caused by gradual thickness inhomogeneities of the samples.

During the data fitting procedure it was found that the fit is insensitive to the effective refractive index as a fit parameter. From Eq. 2.22 is was concluded that this is due to the two issues. Our diffusive absorption length is too large with respect to the extrapolation lengths and the thickness of the samples is in the order of the diffusive absorption length. An important consequence is that we can only determine the value of $\ell_{\text{tr}} + z_{e1}$ and the diffusive absorption length $L_a$.

We have to estimate $n_{\text{eff}}$ because $n_{\text{eff}}$ can not be extracted from the total transmission measurements. We have seen in the SEM images that our samples consists primarily of $TiO_2$ and air, which have refractive indices of 2.7 and 1 respectively. The effective refractive index $n_{\text{eff}}$ can be estimated by assuming the $TiO_2$ has a volume fraction between 0.5 and 0.7. This assumption gives an effective refractive index of $n_{\text{eff}} = 2.0 \pm 0.2$.

With the assumption that the effective refractive index is $2.0 \pm 0.2$, the transport mean free path can be obtained from the fit and we find $\ell_{\text{tr}}$=0.73±0.21 $\mu$m. These values for $\ell_{\text{tr}}$ and $n_{\text{eff}}$ lead to an estimated diffusion constant of 37 $\pm$ 14 $\text{m}^2/\text{s}$. Here we assume that the energy velocity is equal to the phase velocity. The diffusive absorption length is found to be insensitive to $n_{\text{eff}}$, for $L_a$ we found 126 $\mu$m.

From the spread in Fig. 4.3 we see the optical constants differ from sample to sample. In the fit procedure the error of the measurements was not included yet, we only estimated the diffusion constant based on an estimate of the effective refractive index. We will now include the errors in the measurement and describe the fluctuations in the diffusion constant among the different samples.

The error in the fit is estimated by adjusting the fit parameters such that a domain of the fit parameters $\ell_{\text{tr}}$, $n_{\text{eff}}$ and $L_a$ is found in which all the samples fit. These results are shown in Fig. 4.4. The solid line represented the best fit for the data. By decreasing $\ell_{\text{tr}}$ the dashed curve is found, which describes the upper limit in the inverse total transmission. The dotted line shows that the lower limit of the data can be described with a slightly

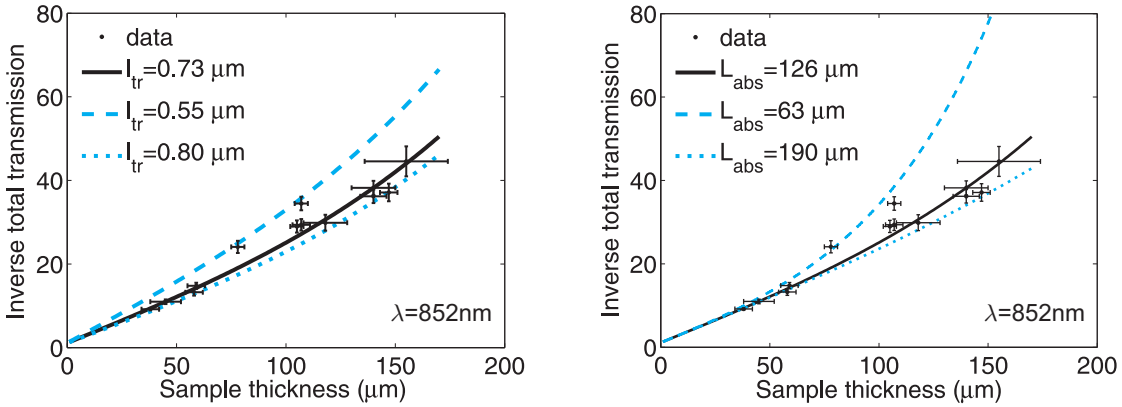


*(a)* *(b)*

*Figure 4.4: (a) To find a range in which all measurements fit, the transport mean free path has to be in between 0.55 µm to 0.80 µm, if the effective refractive index is indeed 2.0. These upper and lower limits for $\ell_{tr}$ correspond to a $n_{eff}$ between 1.8 and 2.1 when the $\ell_{tr}$ is kept fixed. (b) The data is described by an absorption length in the range of 63.2 µm to 190 µm.*

larger $\ell_{\rm tr}$. For the transport mean free path we find a spread of 19 %. Varying the effective refractive index leads to the exact same lines for the dashed and dotted curves, from which we find a spread in the effective refractive index of 8 %. From this information we can estimate that the spread in diffusion constants is 27 %, which means the largest diffusion constant can be 1.7 times the smallest. If we vary the diffusive absorption length such that we can describe all the data points, we find a spread in $L_a$ of 50 %.

We can make a spectrum of both the transport mean free path and the diffusive absorption length, because we have used the Fianium super continuum laser for the total transmission measurements. The spectra for $\ell_{\rm tr}$ and $L_a$ ore obtained by fitting the theory to the data for every wavelength. The two resulting spectra are presented in Fig. 4.5. Both $\ell_{\rm tr}$ and $L_a$ increase smoothly with the wavelength, which indicates resonances do not play an important role. At wavelengths above 800 nm the spectra have quite some noise. The spectra are obtained assuming $n_{\rm eff}$=2.0, which causes a systematic error of 29 %.

When we compare our samples to the ZnO samples characterized previously, we see that in our measurements $\ell_{\rm tr}$ is a lot smaller at 532 *nm* than the ZnO samples. The ZnO sample have $\ell_{\rm tr} = 0.72 \pm 0.18\,\mu$m at 532 nm [16], our samples have $\ell_{\rm tr} = 0.35{\pm}0.10\,\mu$m. The difference is attributed to the high refractive index of $TiO_2$

## 4.5 Conclusions

We tried to make disordered layers of $TiO_2$ particles in the order of 100 $\mu$m thick. We first sprayed the $TiO_2$ pigment on a glass substrate using an airbrush. With this method we did not obtain robust sample with the required thickness. We successfully made samples of the required thicknesses by depositing droplets of paint on the substrate using a pipet. The paint samples are characterized by looking at the structure and the optical properties.

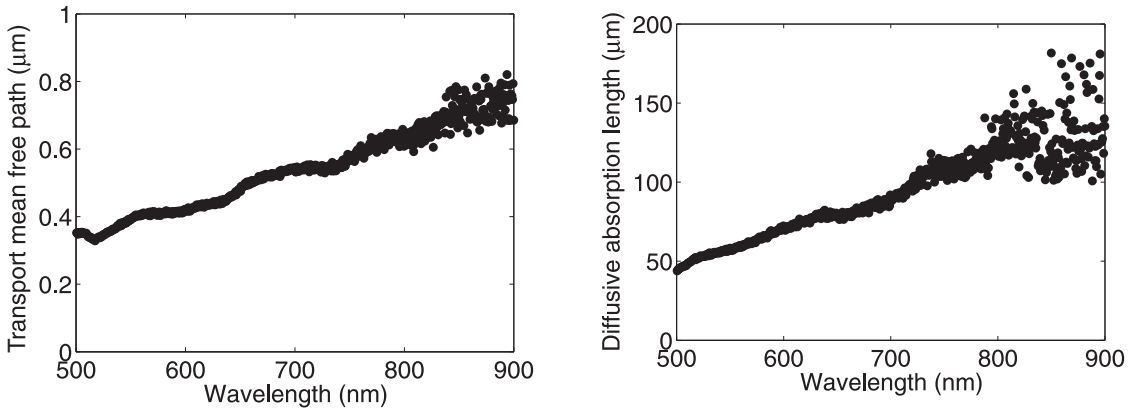


*(a)* *(b)*

*Figure 4.5: (a) The transport mean free path as a function of the effective refractive index for paint samples with an estimated effective refractive index of 2.0. (b) The diffusive absorption length as a function of wavelength.*

At 852 nm a transport mean free path is found of $0.73 \pm 0.21\,\mu$m. From the measurements and the estimated value of the effective refractive index we concluded the diffusion constant has to be $37 \pm 14 \mathrm{m}^2/\mathrm{s}$. Here we assume there are no resonances in the samples. From the fluctuations among the samples, a spread in the diffusion constant is expected of $\pm$ 27%.

# Chapter 5

# Results

## 5.1 Introduction

In Chapter 2 it was predicted that the intensity of an enhanced speckle decays according to the $C^1$ correlation function. An important assumption is that the enhanced speckle is described by transport theory, and thus all paths contribute to the intensity of the enhanced speckle. This assumption is now tested experimentally. It was also shown that a wavefront can be shaped such that the frequency width of an enhanced speckle can be increased of decreased. We will now present the first experiments in which the decay of an enhanced speckles is measured. We also show the first attempts to control the frequency width of the enhanced speckles.

We want to compare the decay of the intensity of an enhanced speckle with the $C^1$ correlation function. To make this comparison we first need to be able to do proper $C^1$ measurements. We will therefore first describe our $C^1$ measurements in Section 5.2. Thereafter our typical measurement procedure is discussed (Section 5.3). In Section 5.4 we present the decay of the intensity of an enhanced speckle due to frequency detuning of the incident light, and we compare the measurements to the experimentally determined $C^1$ correlation function. In Section 5.5 we will show whether the frequency width of enhanced speckles can be controlled.

## 5.2 Measuring $C^1$ correlations

This section introduces a new way of performing $C^1$ measurements. We show that this method accurately determines the $C^1$ correlation function. The method enables us to

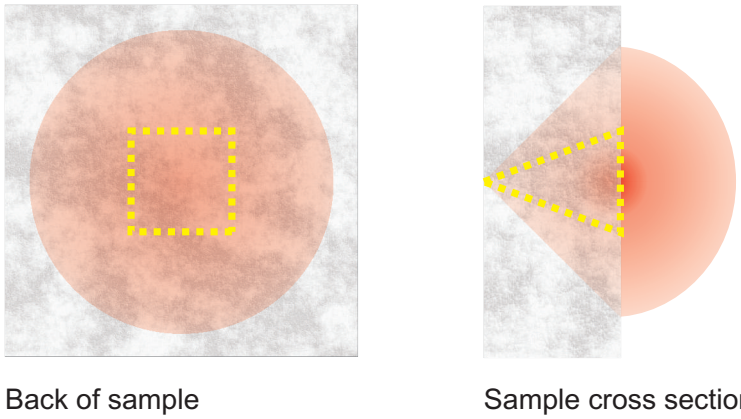


*Figure 5.1: This image shows that various path lengths are selected when several positions are recorded simultaneously. The left hand side shows the selected region. The right hand side shows that the speckles far from the center of the diffusive spot have a longer average path length.*

measure the decay in intensity of the enhanced speckle together with $C^1$.

### 5.2.1 Earlier measurements of $C^1$

In this subsection we review the $C^1$ measurements as they have been performed in the past. In the late 1980's Genack measured $C^1$ correlation functions in the microwave regime [38]. Later $C^1$ correlations were measured in the optical regime by Van Albada *et al.* and De Boer *et al.* [20, 39].

In their measurements of $C^1$ Van Albada *et al.* and De Boer *et al.* focus light on a random sample and image a single speckle spot on a photo detector. Thereafter they scan the laser frequency over a long range. During this scan the intensity fluctuates, from these fluctuations $C^1$ is determined. [20, 39]

By fitting theory to the measured $C^1$ correlation function, and measuring the thickness of the sample, the diffusion constant of the sample is calculated. The theoretical $C^1$ curve assumes one measures the transmission coefficient $T_{ab}$ as a function of $\Delta\omega$ for many sample realizations.

The approach of Van Albada *et al.* and De Boer *et al.* has the advantage all measurements are performed on the same pair of in and outgoing channels. The disadvantage of this system it that one suffers from dispersion of the optical components, due to the long scan range of the laser. Because of fluctuations in the thickness of the sample, Van Albada *et al.* and De Boer *et al.* could not average over different realizations of disorder by moving the sample.

### 5.2.2 Spatially averaged $C^1$ measurement

In this thesis we measure $C^1$ by averaging the intensity over different positions for different frequencies. If one records the entire diffusive spot with a camera, averaging over positions is a quick method, which also allows measuring $C^1$ together with the intensity decay of

the enhanced speckle. It is now discussed whether this method results in an accurate measurement of $C^1$.

In Fig. 5.1 we compare the distance from the ingoing channels to the outgoing channels as a function of the distance from the center of the diffusive spot. We see that the outgoing channels at the edge of the yellow dashed square have a larger distance from the ingoing channel, than the outgoing channels in the center of the square.

For the determination of $C^1$ we average over many different speckles. It is important to average over a sufficient amount of speckles. The number of speckles is determined by the size of the picture we record. Unfortunately for large pictures the distance from source to speckle is much larger for the speckles at the edge of the picture, compared to those at the center of the picture. Moreover large pictures cause the frame rate of the camera to drop, which causes long scan times. Short scan times are important when the system is instable. From the arguments above, we see that the optimum picture size is a trade off between a sufficient amount of speckles, speed and the reliability of the measurements.

To make sure all speckle have equal weights in the correlation, the speckle intensity is divided by the average diffusive background. After this correction the two pictures X and Y can be correlated using:

$$C = \frac{\sum_i X_i Y_i}{\sum_i X_i \sum_i Y_i} - 1, \tag{5.1}$$

where $X_i$ and $Y_i$ are the counts on pixel $i$ divided by the average transmission for that pixel. Determining $C^1(\Delta\omega)$ is done by correlating a picture taken at $\Delta\omega$ with a picture taken at $\Delta\omega = 0$

Using this method, the measured $C^1$ correlation for sample A ($78\pm3\,\mu$m thick) is presented in Fig. 5.2. In the graph we see that the measured correlation is bell shaped and starts at approximately one. The theory (Eq. 2.33) is fitted to the data. The residue (data minus fit) is around zero for all frequency detuning, this shows there is a good fit. From the fit with the experimental data a diffusion constant of $50 \pm 7\mathrm{m}^2/\mathrm{s}$ was extracted. The error in the diffusion constant is caused by the uncertainty in the thickness and the uncertainty in the diffusive absorption length of the sample. The value of the diffusion constant is in agreement with the value of $37 \pm 14\mathrm{m}^2/\mathrm{s}$ we expected from the sample characterization in Chapter 4.

We can conclude that the method we used leads to a $C^1$ correlation which is in good agreement with theory. From this single measurement we can not yet conclude whether this approach leads to a correct value of the diffusion constant.

### 5.2.3 Determining the optimal picture size

In the previous subsection it was stressed that the size of the recorded picture can cause measurement errors in $C^1$. Therefore we will now present measurements showing the influence of the picture size. From these measurements an optimal picture size will be chosen.

Twenty measurements of $C^1$ are performed in which the entire diffusive spot was recorded. The radius of the diffusive spot is proportional to the sample thickness, so to be able to record the entire diffusive spot, a thin sample was used for this measurement

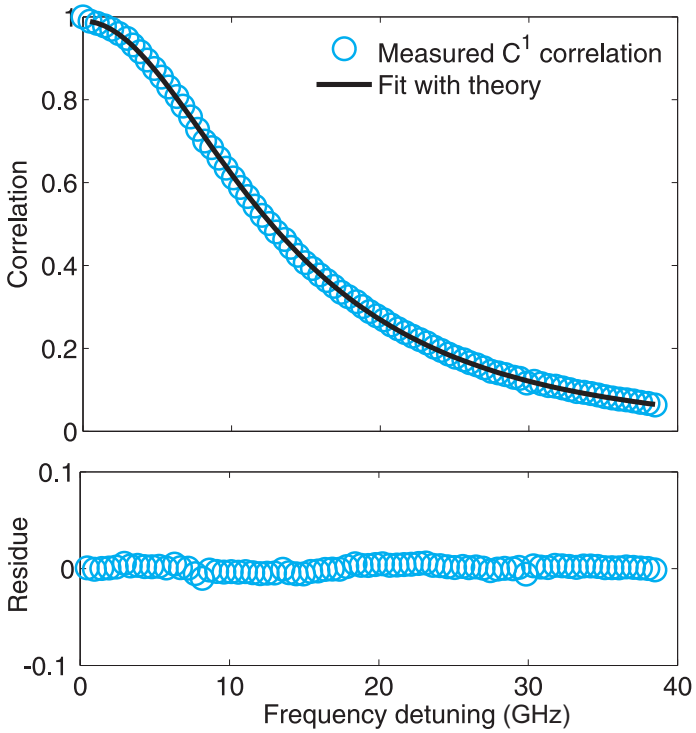


*Figure 5.2: A $C^1$ measurement on sample A (78±3 µm), with fitted theory. The deviations from theory are shown in the residue plot. A diffusion constant of $50 \pm 7 m^2/s$ was extracted from the data.*

(i.e. sample A). By taking subsections of the recorded pictures we varied the picture size with which we determined $C^1$.

The 20 measurements were performed at the same location on the sample, but with different randomly shaped wavefronts. This approach allows us to see whether $C^1$ depends on the shape of the wavefront and whether the measurements reproduce well.

The data has been fitted to Eq. 2.33, where the fit parameter $D/L^2$ can be distinguished. We multiplied Eq. 2.33 with a constant $C_0$, which is the correlation at $\Delta\omega = 0$. Due to noise, $C_0$ will be smaller than one. Both the inverse absorption length $\kappa$ and the momentum difference $\Delta p_\perp$ are set to zero. We can correct for absorption when we extract the diffusion constant.

We expect a large influence of the picture size on the fit parameter $D/L^2$. The upper limit on the picture size will be caused by either the signal to noise ratio, or due to the incorrect value for $D/L^2$. Moreover a lower limit on the picture size is expected, if an insufficient amount of speckles is used for averaging. The lower limit of the picture size can be determined from the reproducibility of the measurements and the residue of the measurements.

**Residue dependence of the picture size**

When the theory is fitted to the data, the residue shows whether the measurements

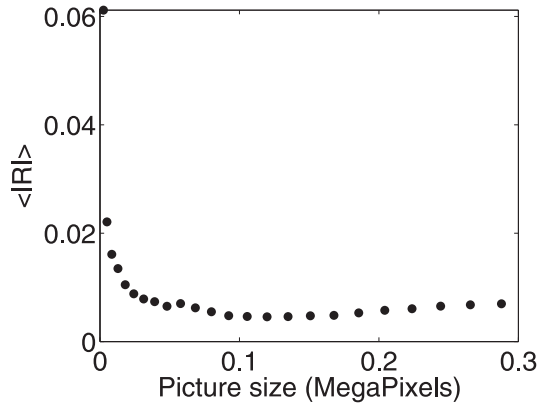


*Figure 5.3: The average value of the residue $|R|$, plotted as a function of picture size. The high residue on for small picture sizes is due to lack of speckles. The high residue on the right hand side is due to the fact that speckles at the edge of the diffusive spot are more sensitive to noise.*

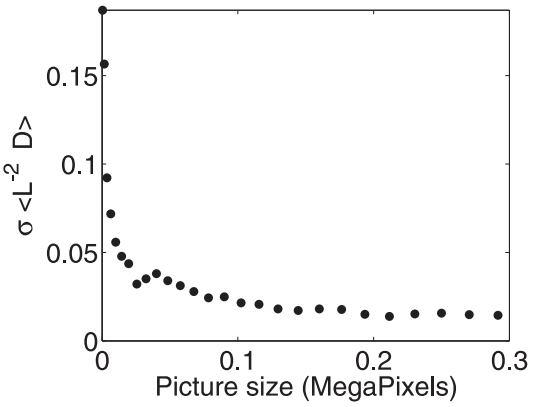


*Figure 5.4: The standard deviation of the fit parameter $L^2/D$ normalized to the fit parameter itself plotted with respect to the picture size. Like the residue, the standard deviation decreases with picture size.*

are well described by theory. The residue is the deviation of the data points from the fit. The average value of the absolute value of the residue, $\langle|R|\rangle$ is an indicator for the fit quality. The fit quality can be poor due to noise, or when the data is not well described by the fitted theory.

The average of $\langle|R|\rangle$ for all 20 measurements is presented in Fig. 5.3 as a function of picture size. For small camera images (up to around 0.02 MegaPixels) the residue is large. This is most likely due to an insufficient amount of speckles used for averaging, and therefore the theory is not suitable for the data. After a minimum of the residue at 0.1 MegaPixel, the residue increases as the picture size increases. Because the speckles far from the center of the diffusive spot have a smaller signal to noise ratio, the increase of the residue after 0.1 MegaPixel is expected to be due to noise.

**Reproducibility as a function of picture size**

The reproducibility of a $C^1$ measurement is determined by looking at the standard deviation of the fit parameter $L/D^2$ of the 20 $C^1$ measurements. The measurements are performed for different wavefronts and on the same location on the sample, therefore the $C^1$ correlation functions are expected to be identical for all these measurements. The standard deviation of $D/L^2$ of the 20 measurements shows to what extend the measurements are identical. The standard deviation of the fit parameter is plotted versus the picture size in Fig. 5.4. For picture sizes larger than 10 KiloPixels, the standard deviation is smaller than 5% of the fit parameter. We take 10 KiloPixels as our lower limit of the picture size. A speckle is estimated to have an area in the order of 10 pixels, thus $1 \cdot 10^3$ speckles would be required for a proper $C^1$ measurement.

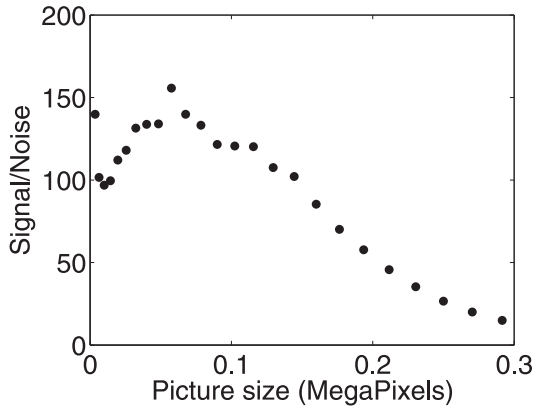


*Figure 5.5: The signal to noise ratio is determined from the value of the fit at $\Delta\omega$=0. The noise level is very good for picture sizes up to 0.1 MegaPixels*

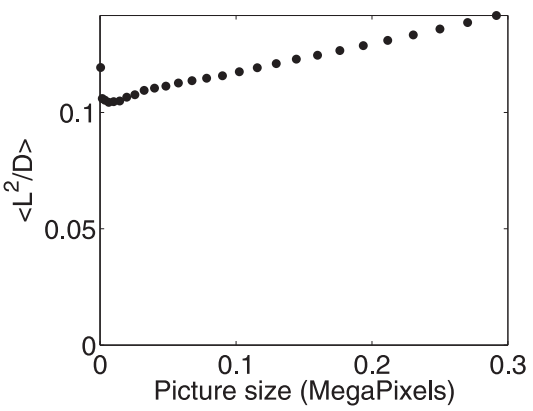


*Figure 5.6: The fit parameter $L^2/D$ increases with picture size. The paths from the source to the edge of the diffusive spot are on average large than those in the center.*

**Signal to Noise ratio as a function of picture size**

The signal to noise ratio of our measurement is presented to see whether the speckles at the edge of the diffusive spot negatively influence the measurement quality. Figure 5.3 indicates that the signal to noise ratio causes an increase of the residue for pictures larger than 0.1 MegaPixels.

The signal to noise ratio can be calculated using the correlation $C$ of two pictures at the same frequency $\omega$ by: $S/N = C/(1-C)$. The fit value at $\omega = 0$ is the average signal to noise ratio of all data points of the $C^1$ measurement. Therefore $C_0 = C^1(\Delta\omega = 0)$ is used to compute the signal to noise ratio. The plot of signal to noise ratio versus picture size shows that the signal to noise ratio is well above 100 for pictures smaller than 0.2 MegaPixels. Therefore we take 0.1 MegaPixels as an upper limit for the picture size.

**Fit parameter $L^2/D$ as a function of picture size**

We expect the fit parameter $L^2/D$ to increase for larger picture sizes. This hypothesis is based on the fact that the light in the speckles at the edge of the diffusive spot is expected to have propagated a large average distance through the material. Figure 5.6 shows that $L^2/D$ indeed increases for larger picture sizes. The behavior at picture sizes smaller than 0.03 Megapixels is expected to be due to poor fits.

One can argue that the increase of the fit parameter $L^2/D$ is not problematic, because the correct fit parameter is the value of the fit parameter at a picture size of zero MegaPixels. To determine $L^2/D$ at zero MegaPixels, one can extrapolate the values of $L^2/D$ between 0.1 and 0.3 MegaPixels to the value of $L^2/D$ at zero MegaPixels.

The effect of the picture size on $L^2/D$ is expected to be smaller for thicker samples. Given the scan range of the laser, sample A (78$\pm$3 $\mu$m thick) is the thinnest sample for which $C^1$ can be measured. Therefore we expect that the overestimation of $L^2/D$ due to

the picture is largest for this sample.

**Conclusion: chosen picture size**

We have shown an analysis of the influence of the picture size on the spatially averaged $C^1$ measurements. We see that for picture sizes under 10 KiloPixels both the residue and the standard deviation of our $C^1$ measurements are unacceptably high. At picture sizes above 0.1 MegaPixels the noise has a strong influence. Because we want to minimize the effect of the increasing value of $L^2/D$ due to the increase of the picture size and we want to allow a large frame rate, we choose a picture size slightly above the minimum picture size. In all our experiments we recorded a picture of 200x200 pixels, thus 0.04 MegaPixels. At this picture size we overestimate $L^2/D$ with maximally 5%, the standard deviation of $L^2/D$ is around 3%.

## 5.3 Procedure

In this section we discuss the different steps which we are done to determine the frequency dependence of the enhanced speckle intensity. In this procedure the measurements of $C^1$ are included. The procedure consists of four steps: generation of the wavefront to create an enhanced speckle, determination of the diffusive background, scanning the laser and last, translation of the sample. These steps will now be discussed in detail.

**1. Generating the wavefront to create an enhanced speckle**

While the laser is locked to frequency $\omega_0$ we generate the wavefront to create an enhanced speckle. A target point is chosen approximately in the center of the diffusive spot at the back of the sample.

A stepwise sequential algorithm [34] is used and repeated three times to generate the wavefront that optimizes the intensity in the target speckle. When the third run of the algorithm leads to no significant improvement of the enhancement compared to the second run, it is certain that the maximum intensity enhancement was obtained given the experimental circumstances in the lab at that time. For most optimizations the speckle intensity after the second run is equal to the speckle intensity in the third run.

In the optimization we used 208 segments. In Chapter 3 it was shown that an average enhancement of 149 can be obtained in good experimental conditions. A run of the algorithm takes two to three minutes.

**2. Determining the average diffusive background**

For the $C^1$ correlations we need to determine the average diffuse intensity $I(x, y)$. Because two different wavefronts lead to two different speckle patterns the average intensity is determined by averaging over many wavefronts. For 500 different wavefronts the entire diffusive spot is recorded. Recording these 500 wavefronts takes around 5 minutes.

**3. Scanning the laser frequency**

In this step we perform the actual measurement of the intensity decay of an enhanced speckle due to frequency detuning, we scan the laser while focussing the optimal wavefront on the sample. During the scan a frame of 200x200 pixels is recorded, where the enhanced

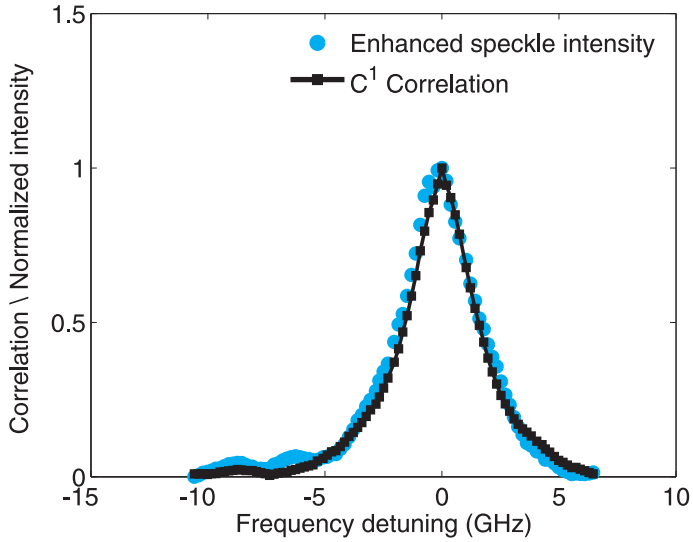


*Figure 5.7: The normalized intensity of the enhanced speckle as a function of frequency detuning $\Delta\omega$. The $C^1$ correlations of all speckles, except the enhanced speckle is presented with black squares and a guide to the eye. The intensity and correlation show identical behavior.*

speckle is at the center of the frame. The peak intensity of the enhanced speckle is used to determine the frequency dependence of the enhanced speckle intensity. The $C^1$ correlation is measured using the other speckles of the recorded pictures. A scan takes 30 seconds, in which approximately 80 frames are recorded. The scan is repeated three times to rule out a measurement in which the laser is not locked properly. Before repeating the scan step two is repeated.

**4. Translating the sample**

The sample is translated 10 $\mu$m after each measurement to obtain statistically independent measurements. Moreover we will obtain scans of enhanced speckles with different degrees of control.

## 5.4 Frequency dependence of the enhanced speckle intensity

In this section we show the first measurements of the decay of an enhanced speckle due to frequency detuning of the incident light. We will first present the typical decay of the enhanced speckle and compare this result to the decay of $C^1$ measurements. Thereafter the statistics of 40 measurements are discussed. We conclude the section with an unexpected phenomenon we observed, namely that the central frequency of the enhanced speckle shifts in time.

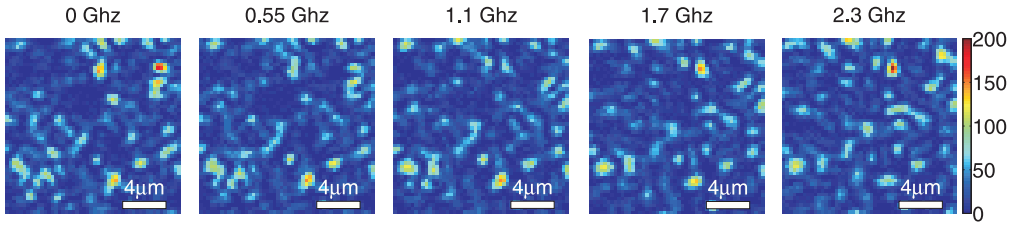


*Figure 5.8: Evolution of regular speckles with changing frequency. The position, size and shape of individual speckles is hard to distinguish.*

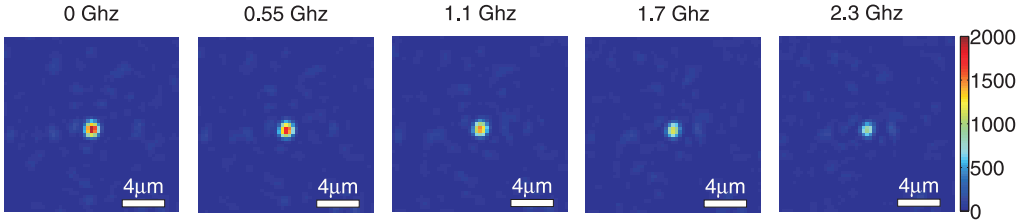


*Figure 5.9: The evolution of an enhanced speckle with frequency. The intensity profile of the speckle is conserved.*

### 5.4.1 Typical measurement on an enhanced speckle

We now present the measurements of the enhanced speckle intensity as a function of frequency detuning. We also show the spatial evolution of the enhanced speckle due to frequency changes.

In Fig. 5.7 the normalized intensity of the optimized speckle (blue dots) as a function of the frequency detuning is plotted together with the measured $C^1$ correlation (black squares). For both the enhanced speckle intensity and the $C^1$ correlation we see the typical bell shape of the $C^1$ correlation. The decay of the enhanced speckle intensity due to frequency detuning is almost identical to the $C^1$ measurement. There are some differences, but these are found primarily in the tail of the intensity decay. The measurement is performed on a single realization of disorder of sample B ($155\pm19\,\mu$m thick), the $C^1$ correlation and intensity decay are measured simultaneously. This experimental result confirms the theory in Chapter 2, which was derived using transport theory.

In the group of Genack (see e.g. [40]) many experiments were performed on the evolution of speckles in space, when the frequency is detuned. We wish to compare these experiments on regular speckles with the behavior of our enhanced speckle. From the experiments of the Genack group it is hard to predict how our enhanced speckle will evolve in space. In Fig. 5.8 we see that regular speckles appear to move and change size, when the frequency is detuned. Therefore it is not excluded that the enhanced speckle moves or changes shape.

The intensity profile of the enhanced speckle is shown Fig. 5.9, as the frequency is detuned. The intensity of the focus drops and the intensity profile is conserved. This shows that the intensity does not move to other outgoing channels when the frequency is

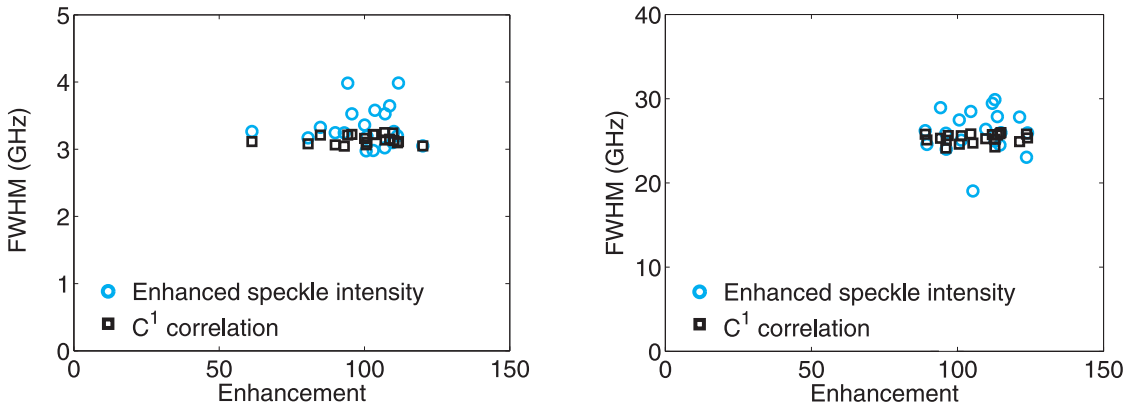


*Figure 5.10: (a) The frequency width of the enhanced speckle is similar to the frequency width of the $C^1$ correlation. The spread in the frequency widths of the enhanced speckle is larger than the spread in the frequency width of the $C^1$ correlation. The frequency width does not depend on the enhancement. Experiments were performed an sample B (155±19 $\mu$m thick) (b) The result in (a) reproduces on the thinner sample A (78±3 $\mu$m thick)*

detuned.

### 5.4.2 Statistics on multiple measurements

In one measurement we have seen that the intensity of the enhanced speckle decays similar to the $C^1$ correlation function. We now repeat this measurement and study the statistics. The different measurements also allow us to see whether the frequency width of the enhanced speckle depends on the degree of control.

The measurement presented in Fig. 5.7 has been repeated for 20 sample realizations of sample B (thickness 155±19 $\mu$m). The frequency width (Full Width at Half Maximum, FWHM) of these 20 measurements is plotted as a function of the enhancement of the speckle in Fig. 5.10(a) There are fluctuations in the frequency width of both the speckles and the $C^1$ correlations. From the measurements in presented in Fig. 5.10(a) it was found that the standard deviation the $C^1$ correlations is 0.07 GHz, where its mean is 3.14 GHz. The standard deviation is around 3%, as expected based on Fig. 5.4. The diffusion constant which can be extracted from this measurement is 22 $\pm$ 10 $m^2/s$, which is in agreement with the sample characterization presented in Chapter 4.

The standard deviation of the frequency width of the intensity enhanced speckles is much larger than the standard deviation of the frequency width of the $C^1$ measurements, namely 0.30 GHz with respect to a mean of 3.32 GHz. In the previous section it was shown that for 1000 speckles, the standard deviation is expected to be around 5% of the frequency width. The enhanced speckle intensity measurements are performed with 208 channels, and therefore stronger fluctuations are expected. Another explanation for the large fluctuations of the frequency width of the intensity enhanced speckle is a frequency

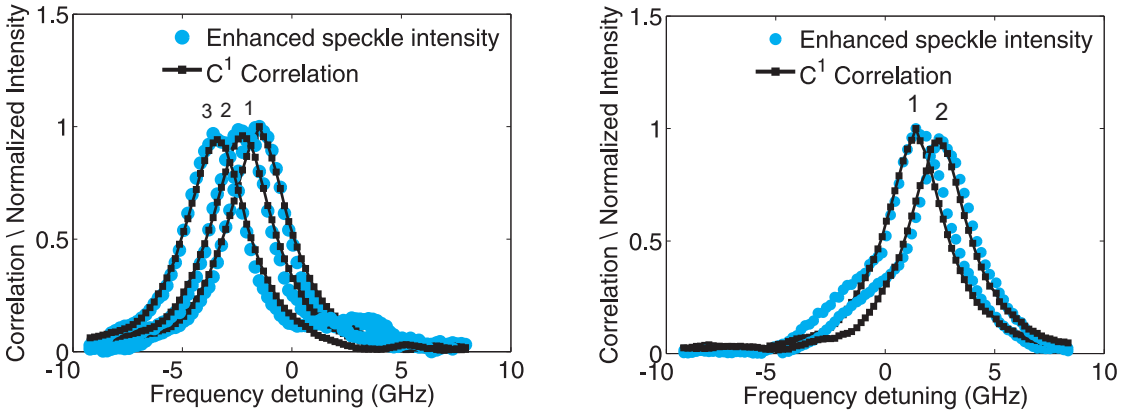


*Figure 5.11: (a) The peak value of the enhanced speckle intensity moves in time towards lower frequencies. The time progression is indicated by the numbers 1, 2, and 3. The peak correlation moves along with the peak of the enhanced intensity. Both the peak correlation and the peak intensity decay in time. (b) The peak can also move towards higher frequencies.*

dependent error term.

The degree of control $\gamma$ varies per measurement due to instabilities (vibrations, temperature drifts) in the set up, which allows us to see whether the frequency width is dependent of the degree of control. The plot in Fig. 5.10(a) shows how the frequency width depends on the enhancement (which is proportional to the degree of control). The frequency width does not depend on $\gamma$ (i.e. the enhancement). This result is also obtained theoretically with transport theory.

We want to check if the result we find for sample B reproduces on sample A. The experiments on sample A ($78\pm3\ \mu$m) are harder because the maximum scan range of the laser is required, which causes it to lose its lock more easily. Moreover the $C^1$ function does not fit entirely in the scan range of the laser. It was possible to optimize speckles and measure the full width at half maximum of the frequency width. Also for this measurement the degree of control varies and a plot of the enhancement versus the FWHM of the frequency width of the enhanced speckle is made.

The result of the experiments on sample A is shown in figure 5.10(b). The experiments on sample A show, exactly like the result on sample B, that the frequency width of the enhanced speckle coincides with $C^1$ and the frequency width is independent of the degree of control. The standard deviation of the $C^1$ correlation is 0.5 GHz with respect to a mean of 25.3 GHz, which cooresponds to the result in Section 5.2. The standard deviation of the frequency width of the enhanced speckle is 2.5 GHz, and its mean is 26.1 GHz.

From the statistics of the measurements on enhanced speckles we have seen that the frequency width does not depend on the degree of control we have over the incident wavefront. This result can also be obtained theoretically using transport theory. The fluctuations observed in the frequency width of the enhanced speckles are considered to be due to a lack of incident channels.

### 5.4.3 Unexpected frequency shifts

We now discuss a striking phenomenon we observed in our measurements. As discussed in the previous section, multiple scans are performed after each other, using the same optimized wavefront. In a few measurements (5% to 15%) a striking effect was observed. The central frequency of the optimized speckle was shown to move in time.

Figures 5.11(a) and 5.11(b) show that the central frequency can both decrease and increase. The peak intensity of the enhanced speckle decays slightly, as the central frequency of the enhanced speckle changes. The background speckles show the same behavior as the enhanced speckle, thus if one records a speckle pattern at frequency $\omega_0$ at time $t_0$, the same speckle pattern appears on a different frequency $\omega_1$ at later in time $t_1$. The maximum correlation decays in time, comparable to the behavior of the peak intensity of the enhanced speckle.

We have checked the Cesium spectra which were recorded for all five measurements in figures 5.11(a) and 5.11(b). Since all the spectra overlap, the absolute frequency of the laser has not changed.

We expect the changes in central frequency to be due to temperature fluctuations in the lab, which cause the sample to expand or contract. If we consider a random scattering sample to be comparable to a fabry perot cavity an expansion or contraction would indeed lead to a change of the central frequency of the peak.

The magnitude of the temperature difference required to obtain this frequency shift can be estimated using the coefficient of linear thermal expansion $\alpha$ of the sample, which is estimated at $50 \cdot 10^{-6}$ K$^{-1}$. If we use $\Delta T = \alpha^{-1} \Delta L/L = \alpha^{-1} \Delta\omega/\omega$, we find 0.05 K to be the temperature change required for the obtained frequency shift. Moreover the relative thickness change would be $3 \cdot 10^{-6}$ which is in the order of a tenth of a nanometer in our samples. The average pathlength difference $\Delta l$ due to the expansion is $2(\Delta L/L)(L^2/\ell_{\mathrm{tr}})$, which is in the order of 50 nm. This distance makes it likely that the thermal expansion causes the shift in central frequency in combination with a small decrease of the correlation peak.

## 5.5 Controlling the phase delay time distribution

In the previous section we have seen that the frequency width of an enhanced speckle is constant within a few percent. The question arises whether the frequency width is fundamental or whether it can be controlled. We presented a method for controlling the phase delay time distribution of an enhanced speckle in Chapter 2. By combining the optimized wavefronts, which were found at different frequencies, the frequency width of enhanced speckle can either be increased or decreased. In this section we will demonstrate whether we control the frequency width of the enhanced speckle, we try to increase and decrease the frequency width.

### 5.5.1 Increased frequency width

We have tried to increase the frequency width of the enhanced speckle by scanning the laser over a range of 3 GHz during the optimization. Because the laser frequency is continuously changing, each segment is optimized at a different frequency. The experiment

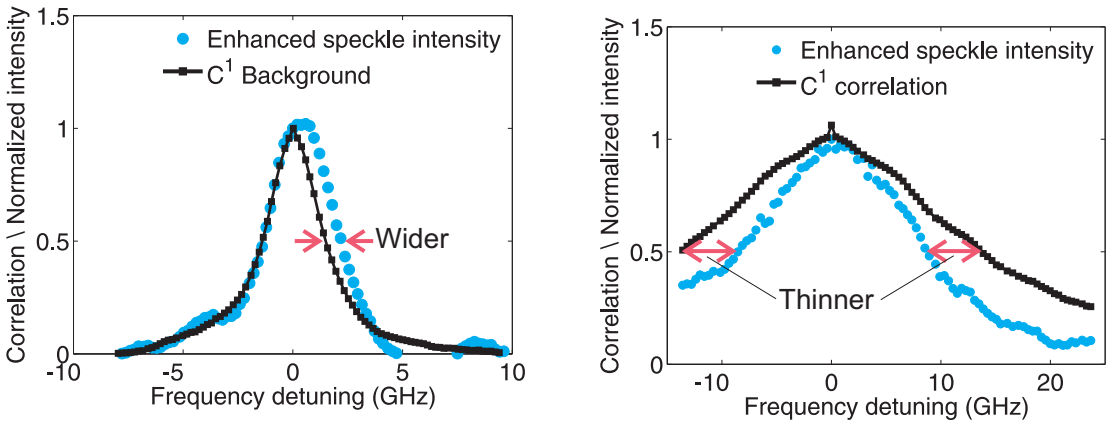


*Figure 5.12: (a) Experimental selection of the small phase delay times. By scanning the laser whilst performing the optimization procedure, the frequency width of an enhanced speckle is increased. The experiment is performed on sample B (thickness 155±19 μm) (b) Experimental selection of large phase delay times. By combining the optimized wavefronts for frequencies detunings 0 GHz, 10 GHz and GHz-10 a decreased frequency width is obtained. The measurement is done on sample A (78±3 μm thick).*

was performed on sample B (155±19 $\mu$m).

The result of the measurement is shown Fig. 5.12(a). We see the $C^1$ correlation, which has its regular shape (black squares). The enhanced speckle has a different shape than $C^1$ and the frequency width of the enhanced speckle is larger. The full width at half maximum is increased to a factor of 1.21 of the width of the $C^1$ correlation. Compared to the measurements presented in Fig. 5.10(a), the increase of a factor 1.21 is approximately two times the standard deviation of the normal fluctuations. The enhancement is reduced to $35 \pm 2$.

### 5.5.2 Decreased frequency width

We performed an attempt to decrease the frequency width of the enhanced speckle. We combine different phase fronts which all lead to an enhanced speckle in the same outgoing channel. The optimizations generating these phase fronts were performed at different frequencies. When combining the phase fronts they were given different weights. The optimization performed at the central frequency was given amplitude one and the other two wavefronts had amplitude -1/2. The optimizations were performed at frequency detunings 0 GHz, 10 GHz and -10 GHz. The experiment was performed on sample A, with thickness 78±3 $\mu$m.

In Fig. 5.12(b) the frequency dependence of a speckle with a decreased frequency width is shown. We see the $C^1$ correlation which does not fit properly in the scan range. The enhanced speckle clearly decays quicker than $C^1$. The frequency width of the speckle is reduced a factor 0.63 of the width of $C^1$. The width is around three times the standard

deviation of the regular fluctuations presented before. The enhancement of the speckle with a decreased frequency width is $39 \pm 2$, which is approximately one third of the enhancement obtained in experiments presented in the previous section.

In the theory chapter it was explained that peaks are expected at 10 GHz and -10 GHz, but these peaks are not found. The observation of these peaks could be prevented due to the fact that they had amplitude half. This means the intensity is four times smaller than the central peak.

## 5.6 Conclusions

In this chapter we presented the first measurements of the intensity decay of an enhanced speckle as a function of frequency detuning. We found a strikingly good agreement between the intensity decay of the enhanced speckle and the measured $C^1$ correlation function. This experiment proves that the theory developed in Chapter 2 is correct.

The measurement was found to reproduce well on 40 different sample realization, 20 realizations on two different samples. For both samples the average frequency width of the $C^1$ correlation is within the standard deviation of the frequency width of the enhanced speckle. The average frequency width of the enhanced speckle is found to be independent of the enhancement, and thus it is independent of the degree of control. This results was also obtained using transport theory.

The standard deviation of the frequency width of the enhanced speckle is four to five times larger than the standard deviation of the frequency width of the $C^1$ correlation. The difference in the standard deviation is most likely caused by the low number of incident channels of the enhanced speckle, compared to the number of outgoing channels we use to measure the $C^1$ correlation.

A striking phenomenon was found when repeating the scan. The central frequency of both the $C^1$ correlation and the enhanced speckle were found to move in time. The peak size of both the $C^1$ and the enhanced speckle also decline in time.

We also showed that wavefront shaping allows us select phase delay times. Control over phase delay times allows one to increase or decreased the frequency width of the enhanced speckle. The frequency width was increased with factor of 1.21 compared to the frequency width of the $C^1$ correlation. An increased frequency width was obtained by tuning the laser during the optimization procedure. The frequency width was decreased by a factor of 0.63 compared to the original frequency width, by combining phase fronts which lead to an enhanced speckle intensity at different frequencies. Controlling the frequency width of the enhanced speckles, leads to a strong reduction of the enhancement.

Chapter 6

# Conclusion

## 6.1 Conclusion

The goal of this thesis is to determine the what the mechanism of wavefront shaping is. In wavefront shaping the light incident on a random scattering material is shaped such that the intensity of a speckle is enhanced. We formulate two different hypotheses exist concerning the mechanism of wavefront shaping. The first hypothesis is that wavefront shaping is described by transport theory, and that all transmission coefficients contribute similar to enhanced speckles, as to regular speckle. The second hypothesis is that the technique selects paths inside the sample, which causes the properties of the transmission coefficients to change.

To test these hypotheses we determined the decay of an enhanced speckle, when the frequency of the incident light is detuned. We first calculated the decay of an enhanced speckle using transport theory. Thereafter, we performed the experiment in which we recorded the decay of an enhanced speckle, when the frequency of the incident light is detuned. This experiment shows whether enhanced speckles are indeed described by transport theory, or whether another mechanism causes the decay of the enhanced speckles.

In our calculations it was shown that the intensity of an enhanced speckle decays, on average, like the $C^1$ correlation function, when the frequency of the incident light is detuned. This result is independent of the enhancement of the speckle, or the degree of control on the incident wavefront. We also showed that the frequency width of an enhanced speckle can be controlled.

To perform our experiments we had to be able to create an enhanced speckle behind samples which are up to 200 transport mean free paths thick. In previous work this was

done in samples up to 40 transport mean free paths. The large sample thickness could cause the technique to fail, because interference is very sensitive to instabilities in the laboratory. We achieved an enhancement close to the predicted value, despite the large sample thickness, temperature drifts, airflow and vibrations.

We measured $C^1$ correlations using a novel technique. We recorded the speckle pattern on the surface of the back of the sample as a function of frequency. We showed that it is possible to measure $C^1$ by correlating the pictures which are taken at different frequencies.

The intensity decay of the enhanced speckle when the frequency of the incident laser light is detuned is measured and compared to the $C^1$ correlation. We found a good correspondence in the functional shape of $C^1$ and the enhanced speckle intensity. We studied the statistics of these measurements on two different samples. These samples have thicknesses $78 \pm 3\mu m$ and $155 \pm 19\mu m$. We found, for both samples, that the full width at half maximum of $C^1$ correlation and the enhanced speckle are almost identical. These measurements also showed that the frequency width is independent of the measured enhancement. These results are in accordance to our calculations, using transport theory.

When performing multiple frequency scans after each other we found a striking phenomenon. The central frequency of both the $C^1$ correlation and the enhanced speckle can move in time. If the central frequency of the enhanced speckle changes the correlation decays slightly. The central frequency can become smaller and larger. The effect is contributed to the thermal expansion of the sample. The relative thermal expansion is estimated to be $3 \cdot 10^{-6}$.

We have demonstrated control over the frequency width of the enhanced speckles. By combining optimal wavefront obtained at different frequencies we have created speckles which are wider and speckles which are thinner than the $C^1$ correlation function. These measurements show that we can control the width of the phase delay time distribution using wavefront shaping.

From the facts that the decay of the intensity of the enhanced speckle is described by the $C^1$ correlation and that the frequency width of the enhanced speckle is independent of enhancement we showed that the behavior of enhanced speckles is described by transport theory. From both our theoretical and experimental findings we conclude that the wavefront shaping method controls diffusive waves, instead of finding shortcut paths through the sample.

## 6.2 Suggestions for improvement

We demonstrated control over the frequency width of the enhanced speckles. These experiments can be explored further. The experiment in which we widened the peak, was performed by scanning the laser during the optimization. When the experiment is repeated it is interesting to combine many wavefronts, for example 10 or 20 wavefronts. Hopefully we can then obtain a speckle of 10 to 20 times the frequency width of $C^1$.

We fitted the measured $C^1$ correlation function to a theoretical function which describes the fluctuations as a function of frequency detuning and a change of the incident angle. The speckles are imaged on the detector and therefore we should use the $C^1$ correlation function for frequency detuning in real space. Here we should also include the effect of the NA of the microscope objective. Using the correct function to fit the data with, leads

to other diffusion constants.

The experiment in which we decreased the frequency width deserves further attention. The frequency at which the wavefronts are generated can be optimized. Moreover we can optimize the amplitudes of the wavefronts. We can also tune the relative phase between the wavefronts. Maybe interesting phenomena are observed when the relative phase between the wavefronts is $\pm\pi/2$ instead of $\pm\pi$.

We have seen that the central frequency of the $C^1$ correlation shifts, and the peak value decays in time. By performing more scans after each other it would be interesting to see how the peak value decays in time. Possibly this decay is described by the $C^2$ correlation. By controlling the temperature of the sample we could be able to prove that the shift in central frequency is due to temperature changes.

## 6.3 Outlook

We have shown that we are able to control the width of the phase delay time distribution. By narrowing the phase delay time distribution the dispersion in a transmitted signal can be descreased. This is relevant if one wants to transmit a signal through a disordered material. To properly transmit a signal, different paths through the sample should approximately have the same length.

We now know that the width of the phase delay time distribution can be controlled. It is interesting to see whether the mean phase delay time can also be controlled, this would mean that the light travels faster or slower through the material. Extending these thoughts, it is maybe possible to bring the light in an Anderson localized mode. Chabanov *et al.* [41] have shown what the statistical behavior of speckles is when light is localized, we could possibly create these statistics with wavefront shaping.

Last, we want to work on an experiment performed earlier, in which it has been shown that the total transmission is increased by enhancing a speckle [27]. It is interesting to see whether this total transmission decays as rapidly as the enhanced speckle. Since $C^2$ describes the fluctuations in the total transmission, one may wonder if the enhanced total transmission decays with $C^2$.

# Bibliography


[1] B. van Tiggelen, *Multiple scattering and the localization of light*, Ph.D. thesis, University of Amsterdam, 1992. — p.11 and 17.

[2] J. F. de Boer, *Optical fluctuations on the transmission and reflection of mesoscopic systems*, Ph.D. thesis, University of Amsterdam, 1995. — p.11, 18, and 22.

[3] I. M. Vellekoop and A. P. Mosk, *Focusing coherent light through opaque strongly scattering media*, Optics Letters **32**, 2309 (2007). — p.11 and 33.

[4] P. Schewe and B. Stein, *Opaque lens*, Physics News Update **835**, 1 (2007). — p.11.

[5] R. Berkovits and S. Feng, *Correlations in coherent multiple scattering*, Physics Reports **238**, 135 (1994). — p.15.

[6] H. C. van de Hulst, *Light scattering by small particles* (Dover, 1981). — p.16.

[7] M. B. van der Mark, *Progation of light in disordered media: a search for Anderson localization*, Ph.D. thesis, University of Amsterdam, 1990. — p.17.

[8] I. M. Vellekoop, *Controlling the propagation of light in disordered scattering media*, Ph.D. thesis, University of Twente, 2008. — p.18, 21, 22, and 44.

[9] B. P. J. Bret, *Multiple light scattering in porous gallium phosphide*, Ph.D. thesis, University of Twente, 2005. — p.18, 19, and 22.

[10] M. P. van Albada, B. A. van Tiggelen, A. Lagendijk, and A. Tip, *Speed of propagation of classical waves in strongly scattering media*, Phys. Rev. Lett. **66**, 3132 (1991). — p.18.

[11] M. Stoerzer, C. M. Aegerter, and G. Maret, *Reduced transport velocity of multiply scattered light due to resonant scattering*, Phys. Rev. E. **73**, 065602 (2006). — p.18.

[12] K. L. van der Molen, *Experiments on Scattering Lasers. From Mie to Random.*, Ph.D. thesis, University of Twente, 2007. — p.18 and 21.

[13] M. U. Vera and D. J. Durian, *Angular distribution of diffusely transmitted light*, Phys. Rev. E **53**, 3215 (1996). — p.19.

[14] A. Lagendijk, R. Vreeker, and P. de Vries, *Influence of internal reflection on diffusive transport in strongly scattering media*, Phys Lett A **136**, 81 (1989). — p.19.

[15] J. X. Zhu, D. J. Pine, and D. A. Weitz, *Internal reflection of diffusive light in random media*, Phys. Rev. A **44**, 3948 (1991). — p.19.

[16] E. G. van Putten, *Focussing of light inside turbid media*, Master's thesis, University of Twente, 2007. — p.20, 29, 39, 44, 47, and 49.

[17] N. Garcia, A. Z. Genack, and A. A. Lisyansky, *Measurements of the transport mean free path of diffusing photons*, Phys. Rev. B. **14492**, (1992). — p.21.

[18] J. Gómes Rivas, *Light in strongly scattering semiconductors, diffusive transport and Anderson localization*, Ph.D. thesis, University of Amsterdam, 2002. — p.21.

[19] I. M. Vellekoop, *Time Resolved Measurements on Diffusion of Light*, Master's thesis, University of Twente, 2003. — p.22 and 47.

[20] M. P. van Albada, J. F. de Boer, and A. Lagendijk, *Observation of long-range intensity correlation in the transport of coherent light through a random medium*, Phys. Rev. Lett. **64**, 2787 (1990). — p.22 and 52.

[21] B. A. van Tiggelen, A. Tip, and A. Lagendijk, *Dwell times for light and electrons*, J. Phys. A Math. Gen. **26**, 1731 (1993). — p.23.

[22] P. Lee, *Universial conductance fluctuations in disordered materials*, Physica A. **140A**, 169 (1986). — p.24.

[23] S. Feng, C. Kane, P. A. Lee, and A. D. Stone, *Correlations and Fluctuations of Coherent Wave Transmission through Disordered Media*, Phys. Rev. Lett. **61**, 834 (1988). — p.24 and 25.

[24] R. Berkovits, M. Kaveh, and S. Feng, *Memory effect of waves in disordered systems: A real space approach*, Phys. Rev. B. **40**, 737 (1989). — p.25.

[25] M. C. W. van Rossum, *Mesoscopic phenomena in multiple light scattering*, Ph.D. thesis, University of Amsterdam, 1995. — p.25.

[26] J. W. Goodman, *Statistical Optics* (Wiley, New York, 2000). — p.26 and 27.

[27] I. M. Vellekoop and A. P. Mosk, *Universal optimal transmission of light through disordered materials*, Phys. Rev. Lett. **101**, 120601 (2008). — p.30, 33, 40, and 67.

[28] I. M. Vellekoop, E. G. van Putten, A. Lagendijk, and A. P. Mosk, *Demixing light paths inside disordered metamaterials*, Optics Express **16**, 67 (2008). — p.33.

[29] E. G. van Putten, I. M. Vellekoop, and A. P. Mosk, *Spatial amplitude and phase modulation using commercial twisted nematic LCDs*, Applied Optics **47**, 2076 (2008). — p.33, 37, and 38.

[30] *Operator's manual, model MBR-110, single frequency Ti:Sapphire laser.* — p.35 and 36.

[31] O. Schmidt, K. M. Knaak, Wynands, and D. R. Meschede, *Cesium saturation spectroscopy revisited: How to reverse peaks and observe narrow resonances*, Appl. Phys. B. **59**, 167 (1994). — p.36 and 37.

[32] T. W. Hänsch, I. Shahin, and A. Schawlow, *High-resolution saturation spectroscopy of sodium D lines with a pulsed tunable dye laser*, Physical Review Letters **27**, 707 (1971). — p.36.

[33] P. J. Harding, *Photonic Crystals modified by optically resonant systems*, Ph.D. thesis, University of Twente, 2008. — p.36.

[34] I. M. Vellekoop and A. P. Mosk, *Phase control algorithms for focusing light through turbid media*, Opt. Comm. **281**, 3071 (2008). — p.40 and 57.

[35] *Hansa Airbrush Pro-color Material Safety Data Sheet.* — p.44.

[36] *Dupont titania dioxide R706 d=360nm.* — p.44.

[37] *Aldrich titanium(IV) oxide -325 mesh, 99+%, Catalog No. 24,857-6.* — p.44.

[38] A. Z. Genack, *Optical transmission in disordered media*, Phys. Rev. Lett. **58**, 2043 (1987). — p.52.

[39] J. F. de Boer, M. P. van Albada, and A. Lagendijk, *Transmission and intensity correlations in wave propagation through random media*, Phys. Rev. B. **45**, 658 (1992). — p.52.

[40] S. Zhang, B. Hu, P. Sebbah, and A. Z. Genack, *Speckle evolution of diffusive and localized waves*, Phys. Rev. Lett. **99**, 063902 (2007). — p.59.

[41] A. A. Chabanov, M. Stoytchev, and A. Z. Genack, *Statistical signatures of photon localization*, Nature **404**, 850 (2000). — p.67.